

Helix breaking transition in the S4 of HCN channel is critical for hyperpolarization-dependent gating.

Marina A. Kasimova*¹, Debanjan Tewari*², John Cowgill*^{2,3}, Willy Carrasquel-Ursulaez², Jenna L. Lin^{2,3}, Lucie Delemotte¹, Baron Chanda^{2,4}

¹ Science for Life Laboratory, Department of Applied Physics, KTH Royal Institute of Technology, Stockholm, Sweden;

² Department of Neuroscience, University of Wisconsin-Madison, 1111 Highland Ave., Madison, WI, 53705

³ Graduate program in Biophysics, University of Wisconsin-Madison

⁴ Department of Biomolecular Chemistry, University of Wisconsin-Madison, 420 Henry Mall, Madison, WI 53706

* equal contribution.

Address correspondence to lucie.delemotte@scilifelab.se or chanda@wisc.edu

ABSTRACT

In contrast to most voltage-gated ion channels, hyperpolarization- and cAMP gated (HCN) ion channels open on hyperpolarization. Structure-function studies show that the voltage-sensor of HCN channels are unique but the mechanisms that determine gating polarity remain poorly understood. All-atom molecular dynamics simulations (~20 μ s) of HCN1 channel under hyperpolarization reveals an initial downward movement of the S4 voltage-sensor but following the transfer of last gating charge, the S4 breaks into two sub-helices with the lower sub-helix becoming parallel to the membrane. Functional studies on bipolar channels show that the gating polarity strongly correlates with helical turn propensity of the substituents at the breakpoint. Remarkably, in a proto-HCN background, the replacement of breakpoint serine with a bulky hydrophobic amino acid is sufficient to completely flip the gating polarity from inward to outward-rectifying. Our studies reveal an unexpected mechanism of inward rectification involving a linker sub-helix emerging from HCN S4 during hyperpolarization.

INTRODUCTION

The hyperpolarization-activated and cyclic nucleotide activated ion channels are found in the pacemaking cells of heart and brain where they play a singular role in regulating rhythmic electrical oscillations (Brown et al., 1979; Ludwig et al., 1998; Santoro et al., 1998). Unlike other members of the voltage-gated ion channel family, these channels open at membrane potentials below the threshold of action potential and depolarize the membrane by increasing the permeability to Na⁺ ions (Brown et al., 1979). Their slow gating kinetics and low permeability determine the frequency of action potential spikes (Larson et al., 2013; Sharpe et al., 2017). In addition to voltage, the gating properties of these channels are regulated by PIP₂ and second messengers such as cAMP which mediates the “fight or flight” response by increasing the activity of HCN channels in sinoatrial nodal cells of the heart (Brown et al., 1979; Pian et al., 2006).

From a structural standpoint, the HCN channels are remarkably similar to other voltage-gated ion channels. They are tetrameric and each subunit consists of the voltage-sensing domain (VSD) (S1-S4 helices) and pore domain (S5-S6 helices) (Lee and MacKinnon, 2017). Like other members of CNBD family, the VSD and pore domain (PD) are arranged in a non-domain swapped arrangement (Lee and MacKinnon, 2017; Whicher and MacKinnon, 2016). The C-linker region connects the cyclic nucleotide binding domain (CNBD) in the carboxy terminal end to the S6 transmembrane segment. The resting state structure of the HCN channel reveals several distinctive features. First, the S4 segment of HCN channel is at least two helical turns longer than the corresponding S4 in depolarization activated ion channels. Second, at the cytosolic amino terminal end, a 45 residue stretch forms a small 3-helix bundle which interacts with the voltage-sensor and CNBD domain. This domain is unique to this

59 channel family and is called the HCN domain. Finally, the S4 helix of HCN channels is in tight
60 juxtaposition with the S5 helix unlike in the related depolarization activated ether-á-go-go (EAG)
61 channel (Lee and MacKinnon, 2017).

62 Recent studies show that the voltage-sensing domains of the HCN channels have an intrinsic
63 ability to drive the channel in both hyperpolarizing and depolarizing directions (Cowgill et al., 2019).
64 This ability to open the channel on hyperpolarization neither depends on the extra length of the S4
65 segment nor on the HCN domain suggesting that there are other non-obvious determinants of gating
66 polarity in the voltage-sensing S4 of HCN channel. Cysteine accessibility studies to probe the nature of
67 these conformational changes show that the S4 undergoes a large downward motion much like the
68 voltage-sensor of the Shaker potassium channel (Bell et al., 2004; Mannikko et al., 2002; Vemana et
69 al., 2004). One notable difference, however, is that the residues in the top part of the S4 helix showed
70 larger displacements compared to those at the lower end. Recently, transition metal FRET studies also
71 propose that the S4 undergoes a downward motion with a slight bend at the tail end of the S4 helix (Dai
72 et al., 2019). Nevertheless, it remains unclear whether these subtle differences in the voltage-sensor
73 motions between outward (depolarization-activated) and inward rectifying (hyperpolarization-activated)
74 channels can account for the distinct gating phenotypes.

75 In order to probe the structural transitions through the gating cycle, we took advantage of the
76 special purpose Anton supercomputer (Shaw et al., 2014) to carry out two independent runs of tens of
77 microseconds long molecular dynamics (MD) simulations. Our simulations showed that the downward
78 movement of the voltage-sensors is accompanied by breaking of the S4 helix into two sub-helices and
79 the lower sub-helix adopting an orientation parallel to the membrane plane and turning into a surrogate
80 S4-S5 linker. To probe the importance of this helix breaking transition, we utilized bipolar chimeras
81 which exhibit both hyperpolarization and depolarization-activated currents (Cowgill et al. 2019). Many of
82 the mutations at this region in the wild type background result in a non-functional phenotype. The
83 bipolar background enables us to robustly quantify the relative contributions of various molecular
84 manipulations on hyperpolarizing vis-à-vis depolarizing currents. Our studies reveal that both the
85 location of the breakpoint and nature of amino acid therein is critical for gating polarity in the channels
86 of this superfamily.

87 **RESULTS**

88 **Atomistic simulations of HCN voltage sensor activation**

89 HCN channels are notoriously slow activating such that even the fastest family members require
90 tens of milliseconds to open. Because this timescale is not accessible in even the most advanced

91 simulations, we employed two strategies to accelerate channel kinetics. First, we applied strongly
92 hyperpolarizing conditions (-550 mV) similar to the approach used for simulations of Kv1.2/2.1
93 deactivation (Jensen et al., 2012). Next, we sought to facilitate the movement of gating charges by
94 further hydrating water crevices inside the voltage-sensing domain (VSD). Inspired by the work of
95 Lacroix *et al.* (2013), we designed a mutant that was anticipated to increase hydrophilicity in the VSD.
96 By comparing the sequences of HCN and EAG homologs, which activate and gate much faster, we
97 identified two positions in S1 with large hydrophobic residues in HCN channels compared to smaller,
98 less hydrophobic residues in the EAG family (Figure 1-figure supplement 1 A, C). Based on this
99 information, we ran preliminary simulations (~ 3 μ s) on the wild-type and mutant (M153T/ I160V) HCN1
100 under hyperpolarizing electric field. In agreement with our prediction, the mutant showed signs of faster
101 activation than the wild type (WT) channel (Figure 1-figure supplement 1 B), therefore we proceeded to
102 run Anton simulations with the mutant channel. Functional testing shows that these mutations are well
103 tolerated (Figure 1-figure supplement 1 D).

104 Substantial conformational change was observed in 6 out of 8 voltage sensors from two
105 independent ~20 μ s simulations of the full length channel (Figure 1 A, B). A large downward movement
106 of the S4 helix drives two positively charged residues across the focused electric field at the charge
107 transfer center (F186) (Figure 1 A, C). This large vertical movement agrees with previous predictions
108 based on cysteine accessibility (Bell et al., 2004; Vemana et al., 2004) and voltage clamp fluorometry
109 (Dai et al., 2019). However, the simulations reveal an unexpected break in the S4 helix, causing the C-
110 terminal half to adopt an orientation parallel the membrane plane (Figure 1 A-E, Video 1) when the last
111 gating charge is transferred. Overlay of 6 independent voltage sensors confirms that they converge to
112 the same activated (Down) structure (Figure 1 B, Figure 1-figure supplement 2). This helix breaking
113 model is in stark contrast to what has previously been observed in simulations of voltage-gated
114 potassium channels and new resting state structures of voltage-gated sodium channels (Delemotte et
115 al., 2011; Jensen et al., 2012; Vargas et al., 2012; She et al., 2018; Xu et al., 2019; Wisedchaisri et al.,
116 2019). In these channels, the consensus view is that S4 moves vertically and twists as a unit in what is
117 typically referred to as the helical screw model (Figure 1E). Interestingly, the structure of the cyclic
118 nucleotide-gated (CNG) channel TAX4 (Li et al., 2017), a close relative to HCN channels (Baker et al.,
119 2015), shows a bent S4 helix reminiscent of what we observe for HCN1 (Figure 1D, E). Thus, the S4
120 segment in these two closely related clades may have an intrinsic propensity to bend.

121 The movement of S4 in response to voltage results in the appearance of gating currents, which
122 has been measured experimentally for the sea urchin HCN (spHCN) channel but not for other HCN
123 channels presumably due to the slow nature of their gating (Ryu and Yellen, 2012). The contribution of

each residue to the net gating charge can be computed from our simulations (Figure 1F, G) (Roux, 2008; Treptow et al., 2009). In this approach, charge contribution of each residue is calculated based on the derivative of the local electrostatic potential with respect to applied voltage in the resting and activated states (the so-called coupling function, Figure 1G). These contributions will only differ between states if either the charged residues move relative to the local electric field or the local electric field rearranges around these residues. Summing the contribution of each residue shows the net gating charge per VSD is 1.85 e_0 (or 7.4 e_0 per channel), which is in good agreement with the 8 charges per channel suggested previously through kinetic modeling of HCN channel activation (Hummert et al., 2018).

As expected, the per-residue contribution to this charge difference is dominated by the two positively charged residues on S4 (R267 and K270) which move relative to the charge transfer center, with lower contributions from the other charges of S4 (Figure 1F). Additionally, the negative countercharges on S1-S3 contribute to the net gating charge as was experimentally shown for the Shaker potassium channel (Seoh et al., 1996). Interestingly, the acidic residues of S1-S3 contribute to the gating charge despite little to no net displacement (Figure 1-figure supplement 2). This implies a redistribution of the local electric field inside the VSD upon activation, as previously suggested based on HCN1 cysteine accessibility studies (Bell et al., 2004). The change in the local electric field can be seen as a change in the coupling function between the activated and resting state (Figure 1G). The local electric field within the VSD is thought to be controlled primarily by hydration of the water accessible crevices (Islas and Sigworth, 2001); as expected, the hydration profile of the VSD is altered upon activation (Figure 1H). It is possible that the increase in hydration of the activated state comes from the mutations we introduced to accelerate gating kinetics. Alternatively, inward movement of the S4 positive charges may cause an increase in hydration of the countercharges on S1-S3 (Seoh et al., 1996). On the internal side, the increased hydration is likely related to the broadening of the internal crevice due to S4 bending. This increase in hydration of the VSD can be tested experimentally using substituted cysteine accessibility.

Helical break model assessed with cysteine accessibility

In substituted cysteine accessibility, cysteines are introduced in specific locations of the channel and their solvent accessibility can be monitored using thiol reactive methanethiosulfonate MTS compounds in a state-dependent manner. From the simulations, we identified positions within the VSD which undergo a predicted change in accessibility to a sphere of 2.9 Å radius (the approximate size of MTSET (2-(trimethylammonium)ethyl methanethiosulfonate)). As expected, many of these positions lie on the S4 helix and have been probed previously (Bell et al., 2004; Vemana et al., 2004). The

experimentally-attained accessibility of most of these residues agree well with the accessibility pattern predicted from our model (Figure 2-figure supplement 1A). A key feature of this pattern is that there is a much larger change in accessibility for the internally accessible residues than external. This indicates that there is a larger conformational change in the internal crevice and lends support to the S4 bending movement observed in our simulations. However, we sought more direct experimental evidence to rule out a canonical vertical S4 movement.

In addition to the state-dependent accessibilities in S4, the simulation also predicts an increase in the accessibility of S1-S3 upon activation. These arise due to broadening of the internally facing crevice and would not be expected if S4 moved vertically as a unit (Figure 2A, B, see also Figure 2-figure supplement 1B, C). Surprisingly, in the activated state models extracted from the simulations, even the charge-transfer center (F186) becomes accessible in 3 out of the 6 activated states (Figure 2C). As the charge-transfer center is often considered the boundary between the internal and external crevices, it is an ideal candidate to test for the crevice broadening predicted in our broken helix model. Due to the high expression levels required for assessing internal accessibility with inside-out patches, we used spHCN rather than HCN1 (Mannikko et al., 2002). The WT spHCN channel shows no detectable functional change following MTSET application to either the closed (depolarized) or open (hyperpolarized) states as has been shown previously (Figure 2D and (Mannikko et al., 2002)). In the charge-transfer center mutant (F186C), internal application of MTSET at depolarized potentials leads to very slowly evolving increase in current amplitude ($\tau_{\text{modification}}=7.5\pm0.5 \text{ M}^{-1}\text{s}^{-1}$). This confirms that the charge-transfer center has low solvent accessibility in the resting state. In contrast, application of MTSET during hyperpolarization results in a rapid increase in peak current amplitude that quickly reaches a steady state ($\tau_{\text{modification}}=440\pm30 \text{ M}^{-1}\text{s}^{-1}$). This more than an order of magnitude increase in accessibility of the charge-transfer center upon channel activation is difficult to reconcile with the helical screw model and supports the helix-breaking model predicted by the simulations.

The crucial role of the S4 breakpoint serine in hyperpolarization-dependent gating

The unique voltage sensor movement we observe in MD simulations naturally raises the question about its role in determining the inverted gating phenotype of HCN channels. To explore this, we took advantage of two previously identified chimeras that only differ in the S3b-S4 voltage-sensing segment, yet show opposite gating polarities (Figure 3A and Cowgill et al., 2019). The HEHEH chimera containing the S3b-S4 voltage-sensing segment from HCN1 activates only upon hyperpolarization while the HEEEH containing the S3b-S4 voltage-sensing segment from the depolarization-activated EAG

188 channel activates only on depolarization. If the helix bending movement underlies inverted gating
189 polarity, we would predict that it is only the lower portion of S4 (lower paddle) that is required for
190 hyperpolarization gating in these chimeras. Indeed, the chimera with only the lower paddle of HCN
191 activates primarily upon hyperpolarization. At depolarized potentials, it conducts a leak current slightly
192 larger than the HEHEH parent (Figure 3-figure supplement 1A-C). On the other hand, the upper paddle
193 chimera activates only upon depolarization and its behavior closely resembles that of the parent
194 chimera with the full EAG voltage sensor. Together, these results suggest that the source of inverted
195 gating polarity can be localized to the lower portion of S4, precisely where we observe the helix break in
196 our simulations.

197 A closer examination of the models from the simulation reveals that the S4 helix breaks in a
198 highly consistent location centered at L271 (Figure 3B, C). Comparison of the consensus sequences for
199 HCN and EAG channels show that this position is predominantly conserved between families. In fact,
200 the overall sequence in this region is very similar between HCN and EAG with the exception of position
201 272. The consensus for HCN channels at this position is polar (such as serine for HCN1) whereas the
202 consensus for EAG is hydrophobic. Furthermore, this residue is situated directly adjacent to the helix
203 break, suggesting it may serve a vital role in channel gating. To test the role of S272 in channel gating,
204 we introduced a series of substitutions (Figure 3-figure supplement 1D) in WT HCN channels. The lack
205 of functional expression of mutants with hydrophobic residues at position 272 indicates that serine is
206 critical for HCN channel gating but we must rule out the possibility that these channels are simply not
207 trafficked to the membrane. As the constructs are C-terminally tagged with mCherry, we can use
208 confocal microscopy to track surface expression. For WT HCN 1, we observe mCherry surface
209 fluorescence from oocytes displaying robust inward currents typical of HCN channels (Figure 3-figure
210 supplement 2A-C). For the hydrophobic mutations, we observe surface fluorescence well above the
211 background of uninjected oocytes, yet do still do not observe currents in these oocytes (Figure 3-figure
212 supplement 2A-C). This confirms that the lack of currents detected in these mutants is a result of
213 abolishment of channel activation in the voltage range tested (-150 mV to 50 mV).

214 Functional experiments in the WT background are difficult to interpret because of confounding
215 issues due to other structural elements in the channel. For instance, we have found that WT HCN
216 channels rapidly inactivate upon depolarization due to the presence of tight interactions at the S4-S5
217 interface (Cowgill et al., 2019). To disentangle these effects and inspired by paddle chimera studies
218 (Alabi et al., 2007), we utilized bipolar constructs such as HHHEH which can activate both upon
219 depolarization or hyperpolarization (Figure 3D). We reasoned that, unlike wild type HCN channels,
220 these channels have the gating machinery to activate in both directions and, therefore, allow us to test

the relative contributions of these substitutions on outward and inward rectification. Strikingly, the S272L mutant is a predominantly outwardly rectifying channel in contrast to the parent HHHEH. We then attempted to rescue the inverted gating polarity phenotype by introducing serines throughout the surrounding region in the S272L background (Figure 3D and Figure 3-figure supplement 1E). Interestingly, only the L271S mutation was capable of restoring a primarily hyperpolarization-activated phenotype like the HHHEH parent (Figure 3D and Figure 3-figure supplement 1E)). This suggests that the location of the serine in the S4 helix is critical for the inverted channel gating phenotype.

Although we were unable to observe the effect of the S272L mutation on HCN1 experimentally, we can assess its influence on channel gating *in silico* using free energy perturbation (FEP) (Rodinger and Pomes, 2005, Zhang et al., 2019). The free energy difference between the activation of HCN1 and its S272L mutant $\Delta\Delta G = \Delta G_{\rightarrow}(mut) - \Delta G_{\rightarrow}(HCN1)$ were calculated using FEP (Zwanzig, 1954) (Figure 4). Considering VSD-only simulations, $\Delta\Delta G$ was estimated via alchemical paths of a thermodynamics cycle as: $\Delta\Delta G = \Delta G_a(HCN1 \rightarrow mut) - \Delta G_r(HCN1 \rightarrow mut)$. In each path S272 was reversibly transformed into a leucine through linear interpolation of the Hamiltonians of the HCN1 and mutant systems, and the free energies of these transformations were then computed using the Bennet Acceptance Ratio method (BAR) (Bennett, 1976). The estimated free energy difference of 0.7 ± 0.4 kcal/mol equates to ~ 2.8 kcal/mol per channel suggesting that the S272L mutation shifts the equilibrium toward the resting state, thus disfavoring activation. The observed difference in free energy is significant because the experimentally determined coupling energy between voltage sensor and pore for spHCN is only 1.3 kT (~ 0.8 kcal/mol) (Ryu and Yellen, 2012)

Hydrophilicity and turn propensity of the breakpoint residue determines gating polarity

We introduced a series of substitutions at S272 for different bipolar backgrounds to better understand the physicochemical underpinnings of gating polarity (Figure 5A and Figure 5-figure supplement 1A-C). Both constructs tested showed a clear trend where hydrophobic substitutions favor depolarization activation while hydrophilic substitutions favor hyperpolarization activation. To quantify the relative strengths of the hyperpolarization and depolarization activation pathways, we used the ratio of the open probability at negative compared to positive membrane potentials ($P_O^{-150 \text{ mV}} / P_O^{50 \text{ mV}}$). This parameter, which we refer to as the gating polarity index, is inversely correlated with residue hydrophobicity with a tight fit (Figure 5B). Previous work on model helices showed that the helical propensity is directly correlated to hydrophobicity in membrane environments (Li and Deber, 1994). Therefore, the negative trend we observed between gating polarity index and hydrophobicity may be caused by the helix-stabilizing nature of hydrophobic residues in transmembrane segments. Indeed, the strong, negative correlation is upheld when comparing the gating polarity index to an experimentally-derived scale for transmembrane helical propensity (Liu and Deber, 1998). Finally, the gating polarity

index shows positive correlation to the independently-derived turn propensity (Monne et al., 1999), which has previously been used as a metric for helix breaking proclivity. Together, these correlations offer strong support for our helix breaking model and reveal that residue polarity at S272 is central to the gating mechanism of HCN channels.

Given the strong effect of the S272 mutants on gating phenotype, we wondered whether introduction of a serine at the equivalent position in EAG channels would be sufficient to confer hyperpolarization activation. The G362S mutant of hEAG shows depolarization-dependent opening with no signs of hyperpolarization activation (Figure 5-figure supplement 1D)). This is not entirely surprising as both HCN and EAG channels have presumably evolved multiple structural elements to favor opening on either hyperpolarization or depolarization. Therefore, we hypothesized that a chimera with minimal components derived from HCN1 (EEHEH) would be especially sensitive to mutations of S272. We refer to this channel as a 'proto-HCN' chimera because it shares some properties of both HCN and EAG channels, which are thought to have evolved from a common ancestor. Remarkably, the leucine, valine, and isoleucine mutations in this background eliminate all detectable hyperpolarization activation in the EEHEH background, transforming an HCN-like parent into an EAG-like channel with a single point mutation (Figure 5C). Thus, divergence of hyperpolarization-activated channels from depolarization-activated channels could have occurred through a single point mutation in the S4 segment.

DISCUSSION

The activation mechanism of HCN channels (Bell et al., 2004; Mannikko et al., 2002; Vemana et al., 2004) involves a movement of S4 analogous to that observed in depolarization-activated channels (Larsson et al. 1996; Ahern and Horn, 2005), but the mechanisms which ultimately lead to inward rectification remains poorly understood (James and Zagotta, 2018). Here, we have resolved the activation pathway of the HCN1 voltage-sensing domain at the atomistic level using multi-microsecond long molecular dynamics simulations starting with the full-length HCN1 resting state structure. We observe that in response to a hyperpolarizing electric field, the S4 positive charges slide down by approximately two helical turns. Coupled to this motion is a $\sim 80^\circ$ bend in S4, which leads the bottom half of this helix to orient itself almost parallel to the membrane plane. Our down state model of the S4 voltage-sensor is consistent with existing S4 cysteine accessibility (Bell et al., 2004; Vemana et al., 2004) and transition metal FRET data (Dai et al., 2019). However, the predicted state-dependent accessibility of the residues in the gating scaffold is incompatible with the classical helical screw motion observed in voltage-gated potassium and sodium channels (Figure 2-figure supplement 1C), see also Pathak et al., 2007). Our studies show that the charge transfer center of HCN channels exhibit a

distinct pattern of accessibility consistent with the molecular simulations. Furthermore, we find that this helix breaking transition is necessary for inward rectification and our studies show that the gating polarity strongly correlates with the energetics of transmembrane helix formation. Strikingly, in a proto-HCN background, the nature of the residue in the S4 breakpoint is the central determinant of gating polarity and the direction of rectification can be switched by a single amino acid substitution.

The mechanism of voltage-sensor activation has been a focus of many studies (Larsson et al., 1996, Chanda et al., 2005; Posson et al., 2005; Long et al., 2007; Swartz, 2008; Delemotte et al., 2011; Henrion et al., 2012; Jensen et al., 2012; Kintzer et al., 2018; Li et al., 2015; Bezanilla, 2018; Wisedchaisri et al., 2019) over the past two decades, and the emerging consensus in the field is that VSD activation involves a helical screw motion across the membrane relative to the surrounding S1-S3 bundle which acts as a gating scaffold. In all these channels, the measured gating charge originates from the physical displacement of S4 in a relatively static electrostatic environment which is also conserved across different voltage sensor domains (Souza et al., 2014). During the gating process, step-wise rearrangement of salt bridges between S4 basic residues and acidic countercharges on S1-S3 (Tao et al., 2010; Pless et al., 2011) facilitates charge transfer from one side to the other. The extent of the S4 motion and the number of rearrangements (termed “clicks”) it undergoes depends, however, on the channel and the magnitude of the electrical force exerted on the S4 positive residues. In part due to lack of structural information, most of the mechanistic studies were focused on outward rectifying ion channels and very little was known about the mechanism of inward rectification. Our simulations based on the high-resolution structure paints an entirely different picture and seems to indicate that at least another type of activation mechanism exists, in which the downward motion of S4 is accompanied by a break in the center of the helix and a change in the electrostatic environment. Whether this activation mechanism is a hallmark found only in HCN channels or is also present in related families remains to be elucidated. Of particular interest now is to understand the activation mechanism in non-domain swapped ion channels activated by depolarization such as hERG and EAG (Trudeau et al., 1995) and examine the role of cytosolic domains in modulating voltage-dependence of activation (Xia et al., 2002; Miranda et al., 2018)

Until recently, all voltage-gated ion channels were also thought to be domain-swapped, with the voltage-sensing domain of one subunit sitting adjacent to the pore domain of its neighboring subunit. Allosteric coupling between the VSD and the pore domain were thought to involve direct contacts between the S4-S5 linker with the C-terminal end of S6 located at the intracellular gating interface (Lu et al., 2002; Soler-Llavina et al., 2006; Long et al. 2007; Muroi et al., 2010, Haddad and Blunck, 2011). The other gating interface involves contacts between the transmembrane residues in the S4 and those

in the neighboring S5 segment (Hou et al. 2017; Fernandez-Marino et al., 2018; Carvalho-de-Souza and Bezanilla, 2019). Recently, several Kv channels including HCN1, EAG and hERG were shown to adopt a non-swapped architecture wherein the VSD of a given subunit is placed next to the pore domain of the same subunit, in an assembly that obviates the need for a S4-S5 linker helix (Lee and MacKinnon, 2017; Wang and MacKinnon, 2017; Whicher and MacKinnon, 2016). Our results provide clues towards elucidating the coupling mechanism between the VSD and the pore domain in HCN channels. While we did not observe pore opening in our simulations, we noticed a consistent motion of S5 in all channel subunits (Figure 6A, B). The S5 N-terminus was displaced away from its original position (Figure 6A), and towards one closer to the putative open conformation of TAX4 and hERG channels (Figure 6 B). Such hinge-like conformational switches are often observed in simulations of channel pores and are thought to be a common mechanism of channel gating (Forrest and Sansom, 2000). An analysis of contacts maintained throughout the simulations showed that the VSD and S5 communicate via two interaction networks (Figure 6C). When the lower S4 sub-helix torques towards the membrane, the S4/S5 interactions at the lower gating interface causes the lower part of the S5 to tilt while the top of the S5 remains anchored in place due to interactions with the relatively static S1 segment at the upper gating interface (Figure 6D). The conservation of contacts explains how spHCN functions as a split channel in which the covalent link between S4 and S5 is severed (Flynn and Zagotta, 2018). We speculate that this splaying of S5 from the central pore in an iris-like motion provides S6 with the space needed for pore opening.

MATERIALS AND METHODS

System preparation for long-timescale molecular dynamics simulation

The structure of the HCN1 apo state (pdb code 5U6O) was used as a starting structure for both Anton runs. Missing residues were built using Modeller (Sali and Blundell, 1993). Additionally, the structure was refined before the second run due to instabilities of several protein domains observed during the first run (see the structure refinement section below). The system for molecular dynamics simulations was prepared using the CHARMM-GUI server (Jo et al., 2008). Briefly, the structure of the HCN1 apo state was embedded in a 1-palmitoyl-2-oleoyl-phosphatidylcholine (POPC) bilayer and solvated in a 150 mM KCl solution. The ions were later removed during the first Anton run, and before the second Anton run, after we noticed that they promoted unpacking of the voltage sensor domains. The CHARMM36 force field (Mackerell et al., 2004) was used for the protein, lipids and ions, and the TIP3P model for water. The M153T/ I160V mutant was built using the mutator plugin of VMD (Humphrey et al., 1996).

Molecular dynamics simulations

355 The initial steps of the WT and M153T/ I160V mutant equilibration were performed on the PDC
356 supercomputer Beskow using Gromacs 2018.1 (Abraham et al., 2015). During these steps (~ 100 ns in
357 total) the restraints applied to the protein were gradually released first from the sidechains and then
358 from the backbone. The simulations were performed in the NPT ensemble; Nose-Hoover thermostat
359 (Nosé, 1984) and Parrinello-Rahman barostat (Parrinello and Rahman, 1981) were used to keep the
360 temperature and the pressure constant at 300 K and 1 bar; the timestep was set to 2 fs.

361 The ~ 3 μ s runs of the WT and the M153T/ I160V mutant systems under an electric field were
362 performed on Beskow using Gromacs 2018.1 (Abraham et al., 2015). The transmembrane potential
363 was then set to 750 mV using the external electric field method. Other simulations parameters were
364 kept identical.

365 The M153T/ I160V mutant system was then transferred to Anton (Shaw et al., 2014) and further
366 equilibrated for ~ 1 μ s. Additional restraints were applied to the hydrogen bonds between the backbone
367 groups of the S4 C-terminus prior to the second long run. These restraints were required to stabilize the
368 secondary structure of the S4 C-terminus that was otherwise partially lost in one of the subunits during
369 the first run. They were completely released after the 600 ns simulation. The simulations were
370 performed in conditions of constant temperature (300 K, Nose-Hoover thermostat (Nosé, 1984)) and
371 pressure (1 bar, MTK barostat (Zhang et al., 2017)). The multigrator approach was used to coherently
372 update the thermostat every 24th step, barostat every 480th step and Newtonian particle motion (Lippert
373 et al., 2013). The timestep was kept to 2 fs.

374 After the equilibration, we gradually increased the transmembrane potential to -750 mV, and to -
375 550 mV in the first and second runs, respectively. In the first run, we then decreased it to -550 mV after
376 ~1.5 μ s. The overall length of the trajectory under an electric field was ~ 18.8 and 22.8 μ s for the first
377 and second runs, respectively. The simulations under transmembrane potential were performed in the
378 NVT ensemble. Other parameters were duplicated from the equilibration.

379 **Structure refinement**

380 During the first Anton run we observed that the HCN domain, the selectivity filter and the A' helix
381 of the C-linker deviated from their initial positions significantly. This instability may result from a
382 relatively low local resolution structure (of the HCN domain specifically), absence of stabilizing factors
383 (cAMP or phosphatidylinositol 4,5-bisphosphate PIP₂ lipids, for instance), dynamic properties of these
384 domains, or other factors. While we cannot rule out all of these possibilities, we were able to test
385 whether alternative modeling of the aforementioned domains in the regions with ambiguous electronic
386 density improved their stability in molecular dynamics simulations during the second Anton run. To do
387 so, we refined the structure using Phenix real-space refinement (Adams et al., 2010) and the cryo-EM
388 map (EMD-8512); 4-fold symmetry was imposed using non-crystallographic symmetry restraints.

Overall 5 macro-cycles were performed with global minimization, local rotamer fitting and simulated annealing. The resulting model was then locally refined using Coot (Emsley and Cowtan, 2004). Briefly, several conformations for the domains regions where the electronic density is ambiguous were generated and refined using real space refinement; torsion, planar peptide and trans peptide restraints were applied, and the refinement weight was set to 40. The model with the best density fit and the smallest number of Ramachandran outliers was further used for the final refinement in Phenix. Simulated annealing was not considered and the remaining settings were identical to that in the first Phenix refinement. The resulting structure was used as a starting point for the second Anton run and is deposited as a part of Supplementary Material.

During the second Anton run the HCN domain and the A' helix of the C-linker were still unstable indicating that their instability potentially finds its origin elsewhere rather than in the modeling of the 3-d structure into the cryo-EM density. These domains partially lost their secondary structure shortly after the restraints on the backbone have been released, similar to what happened in the first Anton run. The selectivity filter, on the other hand, remained stable for a much longer time in the second Anton run (~ 10 μ s compared to only few ns in the first Anton run). After ~ 10 μ s, however, Y361 rotated toward the channel axis and blocked the conductive pore. Similar collapse of the selectivity filter has been observed in other potassium channels at low ionic concentration or in the absence of ionic current (Cuello et al., 2010; Zhou et al., 2001) and has previously been proposed as a mechanism of voltage-dependent gating in K2P channels (Schewe et al., 2016). We hypothesize that while the additional refinement did increase the stability of the selectivity filter other factors such as low ionic concentration or the absence of ionic current resulted in its collapse.

Construction of the multiple sequence alignment

The initial hidden Markov models of the HCN and EAG transmembrane regions were built based on HCN and EAG sequences extracted from the Swiss-Prot database. They were then submitted to HMMER (Eddy, 1995) and iteratively updated with newly identified homologous sequences. Overall 176 and 266 sequences homologous to HCN and EAG channels were found. The resulting multiple sequence alignments were finally used to build sequence logos (Crooks et al., 2004).

Calculation of the gating charge

The per-residue and total gating charge was computed using the “coupling function” method (Roux, 2008; Treptow et al., 2009). In this method, the total gating charge is decomposed into individual contributions from residues as $Q = \sum_j Q^j$, and each contribution is further expressed in terms of the so-called coupling function f :

$$Q^j = \sum_i q_i^j [f_a(r_i^j) - f_r(r_i^j)], \quad (1)$$

421 $f_a(r_i^j)$ and $f_r(r_i^j)$ in Eq. (1) represent dimensionless coupling of the charge q_i^j to the transmembrane
 422 potential V_m in the activated (a) and resting (r) states, and the summation runs over all charges q_i^j of the
 423 j^{th} residue. The coupling function is then approximated as the rate of change of the local electrostatic
 424 potential $\varphi(\mathbf{r})$ with respect to V_m :

$$f_a = \frac{\partial \varphi(\mathbf{r})}{\partial V_m} \approx \frac{(\varphi(\mathbf{r}, V_{m1}) - \varphi(\mathbf{r}, V_{m2}))}{V_{m1} - V_{m2}}, \quad (2)$$

425 where V_{m1} and V_{m2} are two different transmembrane potentials.

426 In practice, from each Anton run under an electric field we extracted ten conformations: five for
 427 the resting state and five for the activated one. For every conformation nine 2 ns molecular dynamics
 428 simulations under different transmembrane potentials were performed. The local electrostatic potential
 429 was then computed for each obtained trajectory using the PME Electrostatics plugin of VMD
 430 (Humphrey et al., 1996). The resulting values were further combined to obtain the coupling function for
 431 each extracted conformation. Finally, the coupling functions were used to compute the per-residue and
 432 total gating charge through Eq. (1).

433 **Calculation of per-residue helicity**

434 Per-residue helicity hp was estimated based on the φ and ψ torsions:

$$hp = (1 + \cos(\varphi - \varphi_\alpha))(1 + \cos(\psi - \psi_\alpha))/4, \quad (3)$$

435 where φ_α and ψ_α are corresponding torsions in a perfect α -helix.

436 **Calculation of solvent accessible surface area (SASA)**

437 Solvent accessible surface area (SASA) was calculated using Gromacs 2018.1 SASA (Abraham
 438 et al., 2015). Radius of the solvent probe was set to 2.9 Å according to the size of MTSET. Renderings
 439 presented in all Figures except 2 and S5 were prepared using Visual Molecular Dynamics VMD
 440 (Humphrey et al., 1996).

441 **Free energy calculations**

442 Free energy perturbation (Zwanzig, 1954) was performed on the voltage sensor domain only
 443 (residues 140-290) on Beskow using Gromacs 2018.1 (Abraham et al., 2015). Representative
 444 conformations of the resting and activated states were extracted from the trajectories under an electric
 445 field, embedded into the system with a POPC bilayer and water, and equilibrated for 100 ns. For the
 446 resting state, 3 conformations were extracted from the equilibration trajectories while for the activated
 447 state we considered 5 conformations spanning its structural diversity. For every conformation the
 448 S272→L transformation was performed through linear interpolation of the Hamiltonians of the systems
 449 with HCN1 voltage sensor and its mutant; λ was used as a coupling parameter such as when $\lambda = 0$ the
 450 Hamiltonian corresponded to the HCN1 system, while when $\lambda = 1$ it was of the S272L system. Overall,
 451 21 consecutive λ windows were considered; in each, the system was first equilibrated for 4 ns and then

the production run was performed during 8-20 ns. The free energy difference and the corresponding error were calculated using the Bennet acceptance ratio method (BAR) (Bennett, 1976) (Supplementary File 1). The free energy difference between the activation of HCN1 and its S272L mutant and the corresponding error are calculated as the average and the standard error based on the 3 to 5 independent estimations.

Molecular Biology

The chimeric constructs were generated between mHCN1 and hEAG1 in pUNIV vector as described previously (Cowgill et al., 2019). Note that although the mouse isoform is used here, we maintain the human HCN1 numbering throughout the figures and text for consistency with the structure and simulations. Additionally, the charge transfer center mutation (F186C) refers to hHCN1 numbering for clarity, which is equivalent to position F260 in spHCN. Site directed mutation was done by Quick Change mutagenesis reaction using a standard protocol. The coding sequences of all constructs were verified using Sanger sequencing. Constructs were linearized with SbfI overnight (15 hours) and transcribed using the T7 mMessage Kit according to the protocol. For experiments requiring inside-out patches, the T7 Ultra kit was used for transcription. RNA was isolated by lithium chloride precipitation and washed with 70% ethanol according to the manufacturer's protocol then resuspended to 1-2 mg/ml using RNase free water.

Recombinant Expression and Electrophysiology

Oocytes were surgically removed from adult *Xenopus laevis* under anesthesia in accordance with the protocol approved by the Animal Care and Use Committee of Wisconsin- Madison at University of Wisconsin-Madison. Stage V-VI oocytes were prepared by treating with 1mg/ml collagenase A (Roche) in a calcium- free ND96 solution for 45 mins to 1 hours until the removal of follicular membrane. The oocytes were stored in ND96 solution with calcium containing BSA (ND96 solution: 96 mM NaCl; 2.5 mM KCl; 1 mM MgCl₂; 5 mM HEPES; 1.8 mM CaCl₂; pH 7.40). Oocytes were maintained in ND96 solution before injection and then transferred to ND96 containing antibiotics (50 µg/ml gentamicin and ciprofloxacin, 100 µg/ml tetracycline, penicillin, and streptomycin) and BSA (0.5 mg/ml) after injections called the post injection solution. Oocytes were injected with 20 – 90 ng of mRNA using Nanoject II (Drummond Scientific). Injections were done in ND 96 without calcium chloride solution. After injection oocytes were kept in the post-injection solution as mentioned above. Two-electrode voltage-clamp (TEVC) recordings were obtained at room temperature with an OC-725C amplifier (Warner) at a sampling rate of 10 kHz. Thin-walled glass pipettes (World Precision Instruments) were used with tip resistances of 0.3 to 0.8 MΩ filled with 3 M KCl. The external solution contains 100 mM KOH, 5 mM NaOH, 20 mM HEPES and 2mM EGTA. Solutions were adjusted to pH 7.4 using methanesulfonic acid. All recordings were obtained with no leak subtraction. Data in Relative

P_O vs. voltage curves were fitted to a sum of two Boltzmann curves in Origin 2017 (OriginLab) with the function $I(V) = O_1 + (A_1 - O_1)/(1 + \exp(k_1(V - V_1))) + O_2 + (A_2 - O_2)/(1 + \exp(k_2(V - V_2)))$, where A₁ and A₂ represent the amplitudes, O₁ and O₂ represent the offsets, V₁ and V₂ represent V_{1/2}, and k₁ and k₂ represent the slope factors for two independent components. As many curves do not reach saturation, curves are primarily provided for visual reference.

Cysteine accessibility experiments

Ionic currents were measured from inside-out patches excised from *Xenopus* oocytes after 1-3 days of mRNA injection. Currents were recorded with an Axopatch 1D amplifier, low-pass filtered at 2 kHz and sampled at 10 kHz. Pipettes were made from borosilicate glass with resistance ranging between 0.7–1.0 MΩ when filled with pipette solution (in mM): 120 KCl, 10 HEPES, and 1.0 CaCl₂, pH 7.2. The intracellular solution contained (in mM): 55 KCl, 5 KF, 10 K₄O₇P₂, 0.1 Na₃VO₄, 10 K₂EGTA, 10 HEPES, diC₈ PIP₂ 100 nM, pH 7.2. KF, 10 K₄O₇P₂ and 0.1 Na₃VO₄ (phosphatase-inhibitors) and diC₈ PI(4,5)P₂ were used. The 1 mM MTSET was prepared by diluting from a 1 M stock prepared daily and stored on ice in internal solution prior to the experiment. Inside-out patches containing sp-HCN channels were exposed to MTSET via a rapid perfusion system in which a computer-controlled valve was used to switch between the internal solution without or with MTSET 1 mM. The dead time of the perfusion apparatus was determined as previously described (Oelstrom et al., 2014) and it was typically 150 ms. This dead time was considered to make the MTSET perfusion coincide with the pulses that open and closed the channels. The time constant of MTSET modification was calculated by fitting peak current at the end of the hyperpolarizing pulse versus the cumulative exposure time to a mono-exponential function. The accessibility (calculated as the apparent second-order rate constants) of MTSET to each cysteine mutant was determined by dividing the reciprocal of the product of the time constant by the MTSET concentration.

Surface expression experiments

Surface fluorescence was measured on a Leica SP8 3X STED Super-resolution microscope using 576 nm excitation and collecting emission from 590-650 nm with a 10X, 1.4 NA objective. Detector gain, pinhole diameter, Z-position, integration time, and all other instrument settings were kept constant between all oocytes measured. Surface fluorescence was defined as the integrated intensity within a box of fixed dimension using ImageJ. Following confocal measurements, oocytes were maintained individually to enable correlation of current recordings to confocal measurements. Currents were recorded in two electrode voltage clamp as described above with the exception that ND96 solution was used externally.

Quantitative and Statistical Analysis

519 Clampfit (Molecular Devices) was used to quantitate currents at steady state. Origin was used to fit
520 data points to a sum of two Boltzmann curves. Kinetic Model Builder was used for all kinetic
521 simulations. PyMOL was used for the structural analysis in Figure 5-figure supplement 1D and USCF
522 chimera for the one in Figure 2. Throughout the paper, n is used to denote the number of oocytes
523 tested in each experiment as indicated in each figure legend.

ACKNOWLEDGEMENTS

This work was supported by grants from the Gustafsson Foundation and Science for Life Laboratory to LD; National Institutes of Health to B.C. (NS101723), J.C. (T32 HL-07936-18), J.L. (T32 GM008293); Anton 2 allocation to B.C. (PSC17025P and PSC18025P); Romnes faculty fellowship to B.C; Science and Medicine Graduate Research Scholars (SciMed GRS) fellowship to J.L. Preliminary simulations and free energy calculations were performed on resources provided by the Swedish National Infrastructure for Computing (SNIC) at the PDC Centre for High Performance Computing (PDC-HPC). Anton 2 computer time was provided by the Pittsburgh Supercomputing Center (PSC) through Grant R01GM116961 from the National Institutes of Health. The Anton 2 machine at PSC was generously made available by D.E. Shaw Research. The authors declare no competing interests. We would also like to thank N. Nallappan and A. Thangaraju for help generating chimeras and A. Thangaraju, N. Nallappan, and W. Stevens-Sostre for performing frog surgeries. We thank Dr. Yuzuru Itoh for help with the structure refinement and Dr. Rebecca J. Howard for assistance in preparing Figure 2. We would like to thank G.A. Robertson for providing hEAG1, C. Czajkowski for providing the pUNIV vector, B. Santoro and S.A. Siegelbaum for providing mHCN1, and U.B. Kaupp for providing spHCN. We would like to thank S. Chowdhury and other members of the labs for helpful discussions and input throughout the project.

545 **REFERENCES**

- 546 Abraham, M.J., Murtola, T., Schulz, R., Páll, S., Smith, J.C., Hess, B., and Lindahl, E. (2015).
547 GROMACS: High performance molecular simulations through multi-level parallelism from laptops to
548 supercomputers. *SoftwareX* 1-2, 19-25.
- 549 Adams, P.D., Afonine, P.V., Bunkoczi, G., Chen, V.B., Davis, I.W., Echols, N., Headd, J.J., Hung, L.W.,
550 Kapral, G.J., Grosse-Kunstleve, R.W., *et al.* (2010). PHENIX: a comprehensive Python-based system
551 for macromolecular structure solution. *Acta crystallographica Section D, Biological crystallography* 66,
552 213-221.
- 553 Ahern, C.A., and Horn, R. (2005). Focused electric field across the voltage sensor of potassium
554 channels. *Neuron* 48, 25-29.
- 555 Alabi, A.A., Bahamonde, M.I., Jung, H.J., Kim, J.I., and Swartz, K.J. (2007). Portability of paddle motif
556 function and pharmacology in voltage sensors. *Nature* 450, 370-+.
- 557 Amaral, C., Carnevale, V., Klein, M.L., and Treptow, W. (2012). Exploring conformational states of the
558 bacterial voltage-gated sodium channel NavAb via molecular dynamics simulations. *Proc Natl Acad Sci*
559 *U S A* 109, 21336-21341.
- 560 Baker, E.C., Layden, M.J., van Rossum, D.B., Kamel, B., Medina, M., Simpson, E., and Jegla, T.
561 (2015). Functional Characterization of Cnidarian HCN Channels Points to an Early Evolution of Ih.
562 *PLoS One* 10, e0142730.
- 563 Bell, D.C., Yao, H., Saenger, R.C., Riley, J.H., and Siegelbaum, S.A. (2004). Changes in local S4
564 environment provide a voltage-sensing mechanism for mammalian hyperpolarization-activated HCN
565 channels. *J Gen Physiol* 123, 5-19.
- 566 Bennett, C.H. (1976). Efficient estimation of free energy differences from Monte Carlo data. *Journal of*
567 *Computational Physics* 22, 245-268.
- 568 Bezanilla, F. (2018). Gating currents. *The Journal of general physiology* 150, 911-932.
- 569 Brown, H.F., Difrancesco, D., and Noble, S.J. (1979). How doew adrenaline accelerate the heart.
570 *Nature* 280, 235-236.
- 571 Carvalho-de-Souza, J.L., and Bezanilla, F. (2019). Noncanonical mechanism of voltage sensor
572 coupling to pore revealed by tandem dimers of Shaker. *Nature communications* 10, 3584.
- 573 Chanda, B., Asamoah, O.K., Blunck, R., Roux, B., and Bezanilla, F. (2005). Gating charge
574 displacement in voltage-gated ion channels involves limited transmembrane movement. *Nature* 436,
575 852-856.
- 576 Cowgill, J., Klenchin, V.A., Alvarez-Baron, C., Tewari, D., Blair, A., and Chanda, B. (2019). Bipolar
577 switching by HCN voltage sensor underlies hyperpolarization activation. *Proc Natl Acad Sci U S A* 116,
578 670-678.
- 579 Crooks, G.E., Hon, G., Chandonia, J.M., and Brenner, S.E. (2004). WebLogo: a sequence logo
580 generator. *Genome research* 14, 1188-1190.

581 Cuello, L.G., Jogini, V., Cortes, D.M., and Perozo, E. (2010). Structural mechanism of C-type
582 inactivation in K(+) channels. *Nature* 466, 203-208.

583 Dai, G., Aman, T.K., DiMaio, F., and Zagotta, W.N. (2019). The HCN channel voltage sensor
584 undergoes a large downward motion during hyperpolarization. *Nat Struct Mol Biol* 26, 686-694.

585 Delemotte, L., Tarek, M., Klein, M.L., Amaral, C., and Treptow, W. (2011). Intermediate states of the
586 Kv1.2 voltage sensor from atomistic molecular dynamics simulations. *Proc Natl Acad Sci U S A* 108,
587 6109-6114.

588 Eddy, S.R. (1995). Multiple alignment using hidden Markov models. *Proceedings International*
589 *Conference on Intelligent Systems for Molecular Biology* 3, 114-120.

590 Emsley, P., and Cowtan, K. (2004). Coot: model-building tools for molecular graphics. *Acta*
591 *crystallographica Section D, Biological crystallography* 60, 2126-2132.

592 Fernandez-Marino, A.I., Harpole, T.J., Oelstrom, K., Delemotte, L., and Chanda, B. (2018). Gating
593 interaction maps reveal a noncanonical electromechanical coupling mode in the Shaker K(+) channel.
594 *Nat Struct Mol Biol* 25, 320-326.

595 Flynn, G.E., and Zagotta, W.N. (2018). Insights into the molecular mechanism for hyperpolarization-
596 dependent activation of HCN channels. *Proc Natl Acad Sci U S A* 115, E8086-E8095.

597 Forrest, L.R., and Sansom, M.S.P. (2000). Membrane simulations: bigger and better? *Curr Opin Struct*
598 *Biol* 10, 174-181.

599 Haddad, G.A., and Blunck, R. (2011). Mode shift of the voltage sensors in Shaker K+ channels is
600 caused by energetic coupling to the pore domain. *The Journal of general physiology* 137, 455-472.

601 Henrion, U., Renhorn, J., Borjesson, S.I., Nelson, E.M., Schwaiger, C.S., Bjelkmar, P., Wallner, B.,
602 Lindahl, E., and Elinder, F. (2012). Tracking a complete voltage-sensor cycle with metal-ion bridges.
603 *Proc Natl Acad Sci U S A* 109, 8552-8557.

604 Hummert, S., Thon, S., Eick, T., Schmauder, R., Schulz, E., and Benndorf, K. (2018). Activation gating
605 in HCN2 channels. *PLoS computational biology* 14, e1006045.

606 Humphrey, W., Dalke, A., and Schulten, K. (1996). VMD: Visual molecular dynamics. *Journal of*
607 *Molecular Graphics* 14, 33-38.

608 Islas, L.D., and Sigworth, F.J. (2001). Electrostatics and the gating pore of Shaker potassium channels.
609 *The Journal of general physiology* 117, 69-89.

610 James, Z.M., and Zagotta, W.N. (2018). Structural insights into the mechanisms of CNBD channel
611 function. *J Gen Physiol* 150, 225-244.

612 Jensen, M.O., Jogini, V., Borhani, D.W., Leffler, A.E., Dror, R.O., and Shaw, D.E. (2012). Mechanism of
613 voltage gating in potassium channels. *Science* 336, 229-233.

614 Jo, S., Kim, T., Iyer, V.G., and Im, W. (2008). CHARMM-GUI: a web-based graphical user interface for
615 CHARMM. *Journal of computational chemistry* 29, 1859-1865.

616 Kintzer, A.F., Green, E.M., Dominik, P.K., Bridges, M., Armache, J.P., Deneka, D., Kim, S.S., Hubbell,
617 W., Kossiakoff, A.A., Cheng, Y., *et al.* (2018). Structural basis for activation of voltage sensor domains
618 in an ion channel TPC1. *Proc Natl Acad Sci U S A* 115, E9095-e9104.

619 Lacroix, J.J., Campos, F.V., Frezza, L., and Bezanilla, F. (2013). Molecular bases for the asynchronous
620 activation of sodium and potassium channels required for nerve impulse generation. *Neuron* 79, 651-
621 657.

622 Larson, E.D., St Clair, J.R., Sumner, W.A., Bannister, R.A., and Proenza, C. (2013). Depressed
623 pacemaker activity of sinoatrial node myocytes contributes to the age-dependent decline in maximum
624 heart rate. *Proc Natl Acad Sci U S A* 110, 18011-18016.

625 Larsson, H.P., Baker, O.S., Dhillon, D.S., and Isacoff, E.Y. (1996). Transmembrane movement of the
626 Shaker K⁺ channel S4. *Neuron* 16, 387-397.

627 Lee, C.H., and MacKinnon, R. (2017). Structures of the Human HCN1 Hyperpolarization-Activated
628 Channel. *Cell* 168, 111-+.

629 Li, M., Zhou, X., Wang, S., Michailidis, I., Gong, Y., Su, D., Li, H., Li, X., and Yang, J. (2017). Structure
630 of a eukaryotic cyclic-nucleotide-gated channel. *Nature* 542, 60-65.

631 Li, Q., Shen, R., Treger, J.S., Wanderling, S.S., Milewski, W., Siwowska, K., Bezanilla, F., and Perozo,
632 E. (2015). Resting state of the human proton channel dimer in a lipid bilayer. *Proc Natl Acad Sci U S A*
633 112, E5926-5935.

634 Li, S.C., and Deber, C.M. (1994). A measure of helical propensity for amino acids in membrane
635 environments. *Nature structural biology* 1, 368-373.

636 Lippert, R.A., Predescu, C., Ierardi, D.J., Mackenzie, K.M., Eastwood, M.P., Dror, R.O., and Shaw, D.E.
637 (2013). Accurate and efficient integration for molecular dynamics simulations at constant temperature
638 and pressure. *J Chem Phys* 139, 164106.

639 Liu, L.P., and Deber, C.M. (1998). Uncoupling hydrophobicity and helicity in transmembrane segments.
640 Alpha-helical propensities of the amino acids in non-polar environments. *The Journal of biological*
641 *chemistry* 273, 23645-23648.

642 Long, S.B., Campbell, E.B., and MacKinnon, R. (2005). Voltage sensor of kv1.2: Structural basis of
643 electromechanical coupling. *Science* 309, 903-908.

644 Lu, Z., Klem, A.M., and Ramu, Y. (2002). Coupling between voltage sensors and activation gate in
645 voltage-gated K⁺ channels. *J Gen Physiol* 120, 663-676.

646 Ludwig, A., Zong, X.G., Jeglitsch, M., Hofmann, F., and Biel, M. (1998). A family of hyperpolarization-
647 activated mammalian cation channels. *Nature* 393, 587-591.

648 Mackerell, A.D., Jr., Feig, M., and Brooks, C.L., 3rd (2004). Extending the treatment of backbone
649 energetics in protein force fields: limitations of gas-phase quantum mechanics in reproducing protein
650 conformational distributions in molecular dynamics simulations. *Journal of computational chemistry* 25,
651 1400-1415.

652 Mannikko, R., Elinder, F., and Larsson, H.P. (2002). Voltage-sensing mechanism is conserved among
653 ion channels gated by opposite voltages. *Nature* 419, 837-841.

654 Miranda, P., Holmgren, M., and Giraldez, T. (2018). Voltage-dependent dynamics of the BK channel
655 cytosolic gating ring are coupled to the membrane-embedded voltage sensor. *eLife* 7.

656 Monne, M., Hermansson, M., and von Heijne, G. (1999). A turn propensity scale for transmembrane
657 helices. *J Mol Biol* 288, 141-145.

658 Muroi, Y., Arcisio-Miranda, M., Chowdhury, S., and Chanda, B. (2010). Molecular determinants of
659 coupling between the domain III voltage sensor and pore of a sodium channel. *Nat Struct Mol Biol* 17,
660 230-U214.

661 Nosé, S. (1984). A unified formulation of the constant temperature molecular dynamics methods. *The*
662 *Journal of Chemical Physics* 81, 511-519.

663 Oelstrom, K., Goldschen-Ohm, M.P., Holmgren, M., and Chanda, B. (2014). Evolutionarily conserved
664 intracellular gate of voltage-dependent sodium channels. *Nature communications* 5, 3420.

665 Parrinello, M., and Rahman, A. (1981). Polymorphic transitions in single crystals: A new molecular
666 dynamics method. *Journal of Applied Physics* 52, 7182-7190.

667 Pathak, M.M., Yarov-Yarovoy, V., Agarwal, G., Roux, B., Barth, P., Kohout, S., Tombola, F., and
668 Isacoff, E.Y. (2007). Closing in on the resting state of the Shaker K(+) channel. *Neuron* 56, 124-140.

669 Pian, P., Bucchini, A., Robinson, R.B., and Siegelbaum, S.A. (2006). Regulation of gating and rundown
670 of HCN hyperpolarization-activated channels by exogenous and endogenous PIP2. *The Journal of*
671 *general physiology* 128, 593-604.

672 Pless, S.A., Galpin, J.D., Niciforovic, A.P., and Ahern, C.A. (2011). Contributions of counter-charge in a
673 potassium channel voltage-sensor domain. *Nature chemical biology* 7, 617-623.

674 Posson, D.J., Ge, P., Miller, C., Bezanilla, F., and Selvin, P.R. (2005). Small vertical movement of a K+
675 channel voltage sensor measured with luminescence energy transfer. *Nature* 436, 848-851.

676 Roderger, T., and Pomes, R. (2005). Enhancing the accuracy, the efficiency and the scope of free
677 energy simulations. *Curr Opin Struct Biol* 15, 164-170.

678 Roux, B. (2008). The membrane potential and its representation by a constant electric field in computer
679 simulations. *Biophys J* 95, 4205-4216.

680 Ryu, S., and Yellen, G. (2012). Charge movement in gating-locked HCN channels reveals weak
681 coupling of voltage sensors and gate. *The Journal of general physiology* 140, 469-479.

682 Sali, A., and Blundell, T.L. (1993). Comparative protein modelling by satisfaction of spatial restraints. *J*
683 *Mol Biol* 234, 779-815.

684 Santoro, B., Liu, D.T., Yao, H., Bartsch, D., Kandel, E.R., Siegelbaum, S.A., and Tibbs, G.R. (1998).
685 Identification of a gene encoding a hyperpolarization-activated pacemaker channel of brain. *Cell* 93,
686 717-729.

687 Schewe, M., Nematian-Ardestani, E., Sun, H., Musinszki, M., Cordeiro, S., Bucci, G., de Groot, B.L.,
688 Tucker, S.J., Rapedius, M., and Baukrowitz, T. (2016). A Non-canonical Voltage-Sensing Mechanism
689 Controls Gating in K2P K⁺ Channels. *Cell* **164**, 937-949.

690 Seoh, S.A., Sigg, D., Papazian, D.M., and Bezanilla, F. (1996). Voltage-sensing residues in the S2 and
691 S4 segments of the Shaker K⁺ channel. *Neuron* **16**, 1159-1167.

692 Sharpe, E.J., Larson, E.D., and Proenza, C. (2017). Cyclic AMP reverses the effects of aging on
693 pacemaker activity and If in sinoatrial node myocytes. *The Journal of general physiology* **149**, 237-247.

694 Shaw, D.E., Grossman, J.P., Bank, J.A., Batson, B., Butts, J.A., Chao, J.C., Deneroff, M.M., Dror, R.O.,
695 Even, A., Fenton, C.H., *et al.* (2014). Anton 2: Raising the Bar for Performance and Programmability in
696 a Special-Purpose Molecular Dynamics Supercomputer. Paper presented at: SC '14: Proceedings of
697 the International Conference for High Performance Computing, Networking, Storage and Analysis.

698 She, J., Guo, J., Chen, Q., Zeng, W., Jiang, Y., and Bai, X.C. (2018). Structural insights into the voltage
699 and phospholipid activation of the mammalian TPC1 channel. *Nature* **556**, 130-134.

700 Soler-Llavina, G.J., Chang, T.H., and Swartz, K.J. (2006). Functional interactions at the interface
701 between voltage-sensing and pore domains in the Shaker K(v) channel. *Neuron* **52**, 623-634.

702 Souza, C.S., Amaral, C., and Treptow, W. (2014). Electric fingerprint of voltage sensor domains. *Proc*
703 *Natl Acad Sci U S A* **111**, 17510-17515.

704 Swartz, K.J. (2008). Sensing voltage across lipid membranes. *Nature* **456**, 891-897.

705 Tao, X., Lee, A., Limapichat, W., Dougherty, D.A., and MacKinnon, R. (2010). A Gating Charge
706 Transfer Center in Voltage Sensors. *Science* **328**, 67-73.

707 Treptow, W., Tarek, M., and Klein, M.L. (2009). Initial response of the potassium channel voltage
708 sensor to a transmembrane potential. *Journal of the American Chemical Society* **131**, 2107-2109.

709 Trudeau, M.C., Warmke, J.W., Ganetzky, B., and Robertson, G.A. (1995). HERG, a human inward
710 rectifier in the voltage-gated potassium family. *Science* **269**, 92-95.

711 Vargas, E., Yarov-Yarovoy, V., Khalili-Araghi, F., Catterall, W.A., Klein, M.L., Tarek, M., Lindahl, E.,
712 Schulten, K., Perozo, E., Bezanilla, F., *et al.* (2012). An emerging consensus on voltage-dependent
713 gating from computational modeling and molecular dynamics simulations. *The Journal of general*
714 *physiology* **140**, 587-594.

715 Vemana, S., Pandey, S., and Larsson, H.P. (2004). S4 movement in a mammalian HCN channel. *J*
716 *Gen Physiol* **123**, 21-32.

717 Wang, W.W., and MacKinnon, R. (2017). Cryo-EM Structure of the Open Human Ether-a-go-go-
718 Related K⁺ Channel hERG. *Cell* **169**, 422-+.

719 Whicher, J.R., and MacKinnon, R. (2016). Structure of the voltage-gated K⁺ channel Eag1 reveals an
720 alternative voltage sensing mechanism. *Science* **353**, 664-669.

721 Wisedchaisri, G., Tonggu, L., McCord, E., Gamal El-Din, T.M., Wang, L., Zheng, N., and Catterall, W.A.
 722 (2019). Resting-State Structure and Gating Mechanism of a Voltage-Gated Sodium Channel. *Cell* 178,
 723 993-1003.e1012.

724 Xia, X.M., Zeng, X.H., and Lingle, C.J. (2002). Multiple regulatory sites in large-conductance calcium-
 725 activated potassium channels. *Nature* 418, 880-884.

726 Xu, H., Li, T., Rohou, A., Arthur, C.P., Tzakoniati, F., Wong, E., Estevez, A., Kugel, C., Franke, Y.,
 727 Chen, J., *et al.* (2019). Structural Basis of Nav1.7 Inhibition by a Gating-Modifier Spider Toxin. *Cell* 176,
 728 702-715.e714.

729 Zhang, H., Jiang, W., Chatterjee, P., and Luo, Y. (2019). Ranking Reversible Covalent Drugs: From
 730 Free Energy Perturbation to Fragment Docking. *Journal of chemical information and modeling* 59,
 731 2093-2102.

732 Zhang, Z., Liu, X., Chen, Z., Zheng, H., Yan, K., and Liu, J. (2017). A unified thermostat scheme for
 733 efficient configurational sampling for classical/quantum canonical ensembles via molecular dynamics. *J*
 734 *Chem Phys* 147, 034109.

735 Zhou, Y., Morais-Cabral, J.H., Kaufman, A., and MacKinnon, R. (2001). Chemistry of ion coordination
 736 and hydration revealed by a K⁺ channel-Fab complex at 2.0 Å resolution. *Nature* 414, 43-48.

737 Zwanzig, R.W. (1954). High-Temperature Equation of State by a Perturbation Method. I. Nonpolar
 738 Gases. *The Journal of Chemical Physics* 22, 1420-1426.

739
 740

FIGURE LEGENDS

Figure 1. Activation of hHCN1 via multi-microsecond long MD simulations. **(A)** (Top) Conformational changes of the hHCN1 voltage sensor triggered by an applied electric field. Representative snapshots of one voltage sensor along the trajectory are shown. The numbers correspond to the timepoints marked on the trajectory plot below. S4 is shown in blue, S3 in gray, S1 and S2 are transparent. (Bottom) Time-dependent displacement of the gating charges along the membrane normal in a representative voltage sensor measured relative to the charge transfer center (F186). **(B)** Overlay of representative structures of six independent activated voltage sensors from two independent ~20 μ s simulation runs. **(C)** Overall displacement of gating charges (S4 basic residues) along the electric field direction. The box plot shows the median, 25-75% (box), 1-99% (bars) of the data collected from the six voltage sensors that underwent activation. **(D)** A comparison of the bend angles of lower S4 sub-helix with the principal axis of the VSDs of HCN and TAX4. HCN1 Up shows the angle between the S4 C-terminus of the HCN1 (PDB 5U6O) and the principal axis of its VSD; HCN1 Down shows the angle between the S4 C-terminus of the simulated structures at the end of the run and the principal axis of its VSD; TAX4 shows the angle between the S4 C-terminus of the TAX4 channel (PDB 5H3O) and the principal axis of its VSD. The box plot shows the median, 25-75% (box), 1-99% (bars) of the data collected from the six voltage sensors that underwent activation. **(E)** Comparison of the VSDs from the hHCN1 activated and resting states, the Kv1.2/2.1 activated and resting state extracted from long timescale simulations (Jensen et al., 2012), and the TAX4 open structure. Small cyan arrows show the displacement of the C α atom of R3 along the applied electric field vector. **(F)** Per-residue gating charge computed per hHCN1 subunit. Positive residues are shown in blue, negative in red and non-charged in orange. Green lines show the cumulative gating charge (thick) and the standard error (thin). **(G)** Coupling function corresponding to the resting (cyan) and activated (red) states. The dashed lines depict the boundaries of the transmembrane part of the voltage sensor. **(H)** Hydration of the HCN1 voltage sensor in the resting (left) and activated (right) states. The shaded regions show, 25-75 (dark) and 10-90 (light) percentiles of the data collected for the six voltage sensors that underwent activation.

Figure 2. State-dependent accessibility of residues in S2 and S4 segments of HCN channel. **(A)** Accessibility of the S2 charge transfer center (Phe residue) in representative molecular models of the activated and resting states Kv1.2/2.1 VSDs and the resting and activated states hHCN1 VSDs extracted from molecular simulations. The charge transfer center is only accessible from the intracellular medium in the activated (Down) state of hHCN1. A cutaway through the VSD is represented as a slightly transparent light brown surface; the charge transfer center (Phe residue) is represented as red spheres. **(B)** Predicted accessibility to internally applied polar cysteine modifying

774 reagents. Accessibility to S4 cysteines will increase in the Down state compared to the Up state for
 775 both models as has been shown previously. The S2 cysteine at or proximal to the charge transfer
 776 center is expected to show very little modification in both Up and Down state in the canonical model.
 777 However, if the helix breaks and opens a large cavity in the Down state, the cysteine at the charge
 778 transfer center will be highly accessible in a state-dependent fashion. **(C)** Solvent accessibility
 779 estimates of S4 (left) and S2 (right) residues for both up and down state models of hHCN1. The
 780 accessibility of each residue is estimated for the six voltage sensors that underwent activation and
 781 shown as one symbol each (closed blue circle for the resting Up state, open orange circle for the
 782 activated Down state). **(D)** State-dependent accessibility of the charge transfer center of
 783 hyperpolarization-activated ion channel. Wild type spHCN channel does not react with MTSET under
 784 hyperpolarized or depolarized condition (top two panels). Substitution of the charge transfer center,
 785 F186C, on the other hand, shows state-dependent reactivity with MTSET (bottom two panels). The rate
 786 of reactivity in the activated Down state is $440 \pm 30 \text{ M}^{-1} \text{ s}^{-1}$ versus 7.5 ± 0.3 in the resting Up state.

787 **Figure 3.** A conserved serine residue (S272) located in the lower half of the S4 segment is critical for
 788 hyperpolarization-dependent gating. **(A)** Cartoon representations and representative current traces for
 789 chimeras with varying contributions of the HCN1 S4 helix. Black traces represent current responses to
 790 depolarizing pulses whereas are red ones depict current responses elicited by hyperpolarizing potential
 791 pulses. Test pulses range from -150 mV to 50 mV from a holding potential of 0 mV (lower paddle), -50
 792 mV (HEHEH), or -90 mV (HEEEH and upper paddle). Scale bars show 5 μA (vertical) and 200 ms
 793 (horizontal). Color coding and scale bars are same throughout the figure. **(B)** Top: Consensus
 794 sequences from multiple sequence alignments for S4 helix of EAG and HCN families shown as
 795 sequence logos (Crooks et al., 2004). The height of each residue is proportional to its frequency, while
 796 the height of the overall stack of residues is inversely proportional to Shannon entropy. Bottom: Helicity
 797 of S4 helix plotted as a function of residue position in the activated state of HCN1 from simulations. The
 798 box plot shows the median, 25-75% (box), 1-99% (bars) of the data collected from the six voltage
 799 sensors that underwent activation. **(C)** Structure of a representative activated state model highlighting
 800 the position of key residues near the bend (L271 and S272 in gray and green sticks, respectively). **(D)**
 801 Left: Representative current traces from the bipolar chimera HHHEH and mutants of this background
 802 near the site of the S4 bending. Test pulses range from -150 mV to 50 mV from a holding potential of -
 803 50 mV (HHHEH and L271S+S272L) or -100 mV (S272L). Right: Relative P_O vs. voltage curves for the
 804 mutants. Error bars represent standard deviation $n = 4$ (S272L), 4 (S271S+S272L) from independent
 805 measurement.

Figure 4. Contribution of the breakpoint serine to the free energy of activation of the HCN1 VSD. The thermodynamic cycle shows the activation of HCN1 and its S272L mutant ($\Delta Gr \rightarrow (mut)$ and $\Delta Gr \rightarrow a(HCN1)$), and the alchemical paths of S to L transition in the two VSDs ($\Delta Ga(HCN1 \rightarrow mut)$ and $\Delta Gr(HCN1 \rightarrow mut)$). The mutated residue is colored in green.

Figure 5. The physicochemical property of residues at the breakpoint is the primary determinant for gating polarity in HCN-EAG chimeras. **(A)** Left: Representative current traces of the parent HHHEΔC SD (serine) and S272 mutants from two-electrode voltage clamp arranged according to decreasing hydrophobicity. The SD mutations are the same described previously (Cowgill et al., 2019). Black traces represent current responses to depolarizing pulses whereas red ones depict current responses elicited by hyperpolarizing potential pulses. Test pulses range from -150 mV to 50 mV from a holding potential of -50 mV (Glutamine), -60 mV (Serine), or -90 mV (Leucine, Valine, and Alanine). Scale bars show 5 μA (vertical) and 200 ms (horizontal). Right: Relative P_O vs. voltage curves for the mutants presented on the left. The relative P_O -V curve for the parent HHHEΔC-SD is shown as a blue line. Error bars represent standard deviation from n= 6 (Leucine), 5 (Alanine and Valine), 4 (Proline) from independent measurements. **(B)** Correlation of gating polarity index ($P_O^{-150 \text{ mV}}/P_O^{50 \text{ mV}}$) and Kyle-Doolittle hydrophobicity (left), helical propensity (middle), and turn propensity (right) for the HHHEΔC SD. **(C)** Left: Representative current traces of the parent EEHEH (serine) and hydrophobic substitutions at S272 position. The traces are colored as described earlier. Pulse protocol is from -150 mV to 50 mV from holding potential of -40 mV (EEHEH) or -100 mV (all others). Scale bars show 2 μA (vertical) and 200 ms (horizontal). Right: Relative P_O vs. voltage curves for the mutants presented on the left. The relative P_O -V curve for the parent EEHEH is shown as a blue line. Error bars represent standard deviation n= 5 (Leucine and Isoleucine), 4 (Valine) from independent measurement.

Figure 6. Possible mechanism of hyperpolarization-dependent opening. **(A)** Conformational rearrangements of S4 and S5 during activation. At the end of the simulations, the C-terminus of S4 (shown in dark blue for the resting Up state and in light blue for the activated Down state) is parallel to the membrane which causes the S5 helix (dark red for the resting Up state and in light red for the activated Down state) to tilt at the bottom. S5 helices of other subunits and S6 are shown as transparent helices for context. **(B)** Root mean square deviation (RMSD) of the S5 (top) and S6 (bottom) of HCN1 before (stars) and after (boxplots) MD simulations. HCN1 closed shows the RMSD values with respect to the initial structure of HCN1 (PDB 5U6O); TAX4 open shows the RMSD values with respect to the structure of TAX4 (PDB 5H3O); hERG open shows the structure of RMSD values with respect to the structure of hERG (PDB 5VA1). The arrows indicate the direction along which the HCN1 conformation evolves during activation. For instance, in case of S5, it diverges from the

839 conformation in the HCN1 structure, and approaches that in TAX4 and hERG. **(C)** Network of
840 interactions between the voltage sensor and the pore domain observed in the MD simulations (yellow),
841 separated into two groups: between the C-termini of S1 and S5, and between the C-terminus of S4 and
842 the N-terminus of S5. **(D)** Suggested model for coupling between the voltage sensor and the pore
843 domain of HCN1. Upon activation, S4 (blue) pulls the N-terminus of S5 (green) through the first
844 interaction network. The other interaction network anchors the C-terminus of S5 to a static S1 (yellow).
845 These motions create room for S6 rearrangement and allow it to relax to an open conformation.

SUPPLEMENTAL FIGURE LEGENDS

Figure 1- figure supplement 1 Design and model of an HCN1 mutant with faster activation kinetics.

(A) Consensus sequences from multiple sequence alignments for the voltage sensor of the EAG and HCN families shown as sequence logos (Crooks et al., 2004). The height of each residue is proportional to its frequency, while the height of the overall stack of residues is inversely proportional to Shannon entropy. Residues facing the interior of the voltage sensor are highlighted with gray rectangles. Candidate residues for mutations were chosen according to two criteria: they were hydrophobic and facing the VSD hydrated lumen in HCN1, and substitution to hydrophilic residues were tolerated in the EAG family. The mutated residues are marked with stars. **(B)** Z-position (along the membrane normal) of R270 relative to the charge transfer center residue (F186) along simulation time in the HCN1 wild type (cyan) and mutant (red). Each subunit is shown as a separate trace. **(C)** Cartoon representation of the voltage sensor with the two mutated residues (red). R270 and the hydrophobic plug (F186) used to monitor activation kinetics (see panel B) are shown in green. **(D)** Top: Example traces of the M153T/I160V mutant (right) compared to wild type HCN1 (left). Black traces represent current responses to depolarizing pulses whereas red ones depict current responses elicited by hyperpolarizing potential pulses. Test pulses range from -150 mV to 50 mV from a holding potential of -10 mV. Scale bars show 2 μ A (vertical) and 200 ms (horizontal). Bottom: Relative open probability vs. voltage relationships for the wild type (blue line) and mutant channel (red) with error bars showing standard deviation from 3 independent measurements.

Figure 1- figure supplement 2 Activation of the six voltage sensor domains observed in two independent MD simulations. **(A)** Z-position of gating charges (K261, R267, R270, R273, R276) and their negative counterparts (D183, D189, D233, D255) with respect to the hydrophobic plug (F186) along simulations time. **(B)** Representative conformations of the activated voltage sensor domains highlighting the localization of the residues presented in panel A.

Figure 2- figure supplement 1 Activated state model explains state-dependent accessibility of S4 residues. **(A)** Comparison of solvent accessibility data reported by (Bell et al., 2004; Vemana et al., 2004) (left plot) and calculated from the MD simulations (right plot). Solvent accessibility is estimated experimentally as a rate of modification by MTSET and in the simulations as the surface area accessible to MTSET (SASA). For the simulations, the data was collected from the six voltage sensors that underwent activation; each data point corresponds to the average SASA estimated for one voltage sensor. The values for the resting (Up) state are shown as filled cyan circles, and those for the activated (Down) state as open red circles. **(B)** Models of the voltage sensor domains in the resting

880 (Up) and activated (Down) conformations with residues in panel A highlighted. Residues accessible in
 881 both states are colored in cyan, and residues accessible mostly in the activated state are colored in red.
 882 **(C)** A cartoon highlighting the key features of the two possible models for hyperpolarization-dependent
 883 gating. In the canonical helical screw motion, the S4 translates across the membrane in a helical screw
 884 motion, past the charge transfer center within the gating scaffold. Our MD simulations of HCN channels
 885 show that the S4 helix moves down and breaks into two parts with the lower helix becoming almost
 886 parallel to the membrane.

887

888 **Figure 3- figure supplement 1** Probing the role of HCN S4 in hyperpolarization dependent gating. **(A)**
 889 Snake plot of the mouse HCN1 sequence showing the various breakpoints used for designing the
 890 chimeras. **(B)** Relative P_O vs. voltage curves for the HEHEH and HEEEH chimeras, and the lower and
 891 upper paddle mutants. The parent HEHEH and HEEEH are shown as lines for clarity. Error bars
 892 represent standard deviation. **(C)** Sequence alignment of hHCN1, mHCN1, hEAG1 and rEAG1 showing
 893 the sequence used in the lower and upper paddle chimeras. **(D)** Wildtype HCN1 with different
 894 mutations at S272 position. Black current traces are elicited by pulses to depolarizing potentials
 895 whereas are red current traces are elicited by pulses to hyperpolarizing potentials. Scale bars represent
 896 5 μ A (vertical) and 200 ms (horizontal). Color coding and scale bars are same throughout the figure.
 897 Test pulses range from -150 mV to 50 mV from a holding potential of -10 mV. Right: Relative P_O vs.
 898 voltage curves for the mutants presented on the left with WT HCN1 shown as a line for clarity. Error
 899 bars represent Standard Deviation from n= 4 (Glycine and Alanine), 5(WT HCN1), 6 (Proline) from
 900 independent measurements. **(E)** Sequences of the S4 segment of the HHHEH chimera and its mutants
 901 S272L, L271S/S272L, S272L/L274S and S272L/I275S. **(F)** Representative current traces for the
 902 HHHEH chimera and its mutants S272L/L274S and S272L/I275S. Test pulses range from -150 mV to
 903 50 mV from a holding potential of -80 mV. Right: Relative P_O vs. voltage curves for the mutants
 904 presented. Error bars represent Standard Deviation from n= 4 (S272L/S274S), 5 (S272L/I275S) from
 905 independent measurements.

906

907 **Figure 3- figure supplement 2** Surface trafficking of HCN1 and hydrophobic mutants at S272 **(A)**
 908 Correlation of maximum current amplitude with mCherry surface fluorescence for HCN1 WT,
 909 hydrophobic mutants at S272 and uninjected oocytes. Each point represents the maximal current
 910 amplitude and integrated surface fluorescence of one oocyte. **(B)** Current-voltage relationships for the
 911 oocytes tested in (A) shown with the same color scheme. Error bars represent SEM for 3 oocytes (or 2
 912 oocytes for uninjected). **(C)** Representative confocal micrographs of oocytes used in previous panels.

913

Figure 5- figure supplement 1 Bipolar chimeras point to the outstanding role of S272 for hyperpolarization dependent gating. **(A)** Top: Representative current traces for the HHHEH chimera and its single point mutants. Black current traces are elicited by pulses to depolarizing potentials whereas red current traces are elicited by pulses to hyperpolarizing potentials. Test pulses range from -150 mV to 50 mV from a holding potential of -40 mV (Histidine, Glutamine, Alanine, Glycine), -50 mV (Serine), or -100 mV (Isoleucine, Valine, Proline). Scale bars represent 5 μ A (vertical) and 200 ms (horizontal). Color coding and scale bars are same throughout the figure. Bottom: Relative P_O vs voltage plots for the S272 mutants in the HHHEH background. The black trace in each plot represents the original chimera with a serine at 272. Error bars represent Standard Deviation from n= 3 (Isoleucine and Histidine), 4 (Proline, Alanine and Glutamine) and 6 (Valine) from independent measurements. **(B)** Gating polarity index ($P_O^{-150\text{ mV}}/P_O^{50\text{ mV}}$) were plotted against the transmembrane helical propensity (left), Kyle-Doolittle (KD) hydrophobicity index (middle), and turn propensity (right) of amino acids according to those described previously (see Figure 5). **(C)** Representative current traces for the HHHE Δ C SD chimera and its single point mutants. Test pulses range from -150 mV to 50 mV from a holding potential of -40 mV (Glycine) or -90 mV (all others). Bottom: Relative P_O vs voltage plots for the S272 mutants in the HHHE Δ C SD background. Error bars represent Standard Deviation from n= 5 (Histidine, Asparagine and Glycine), 6 (Leucine and Phenylalanine), or 4 (Proline) independent measurements. **(D)** Left: Structural overlay of the hHCN1 and rEAG voltage sensors with the position of G362 highlighted as spheres. Middle: Representative current trace for hEAG G362S measured in two-electrode voltage clamp. Due to the high conductance of this mutant at negative membrane potentials, current recordings in high external potassium resulted in clamp errors, thus ND96 solution was used externally (2 mM potassium). Right: Open probability vs. voltage relationships for hEAG and the G362S mutant. Error bars represent standard deviation.

Video 1

Conformational changes of the HCN1 voltage sensor during activation. The S4 helix is shown in cyan, its positively charged residues in different colors (K261 purple, R267 cyan, R270 green, R273 orange and R276 red). The hydrophobic plug (F186) is colored in light green. S3 is gray and the rest of the voltage sensor is transparent.

Supplementary File 1

Free energy differences for different replicates of the S to L alchemical transformations of the HCN1 VSD.

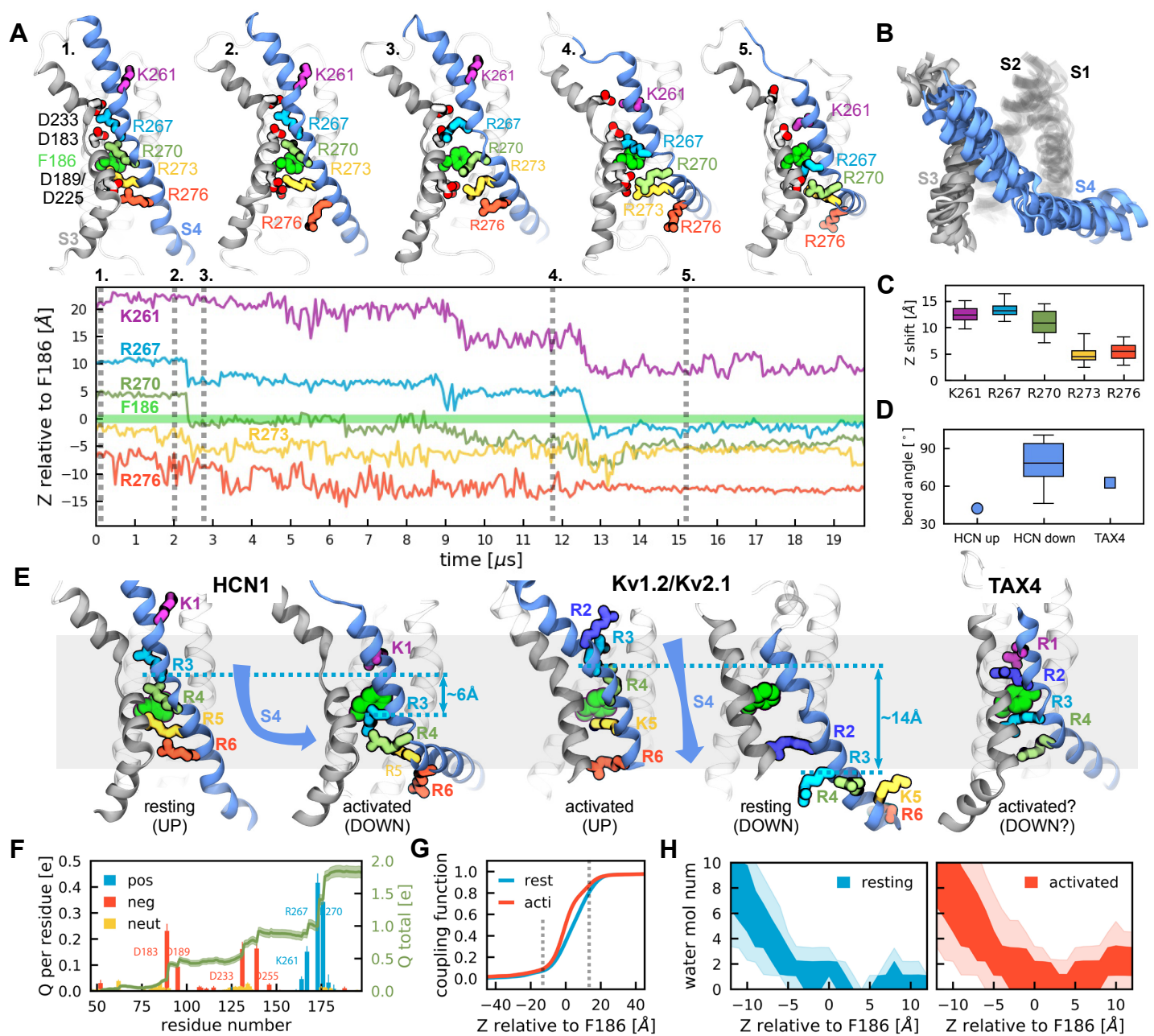


Figure 1

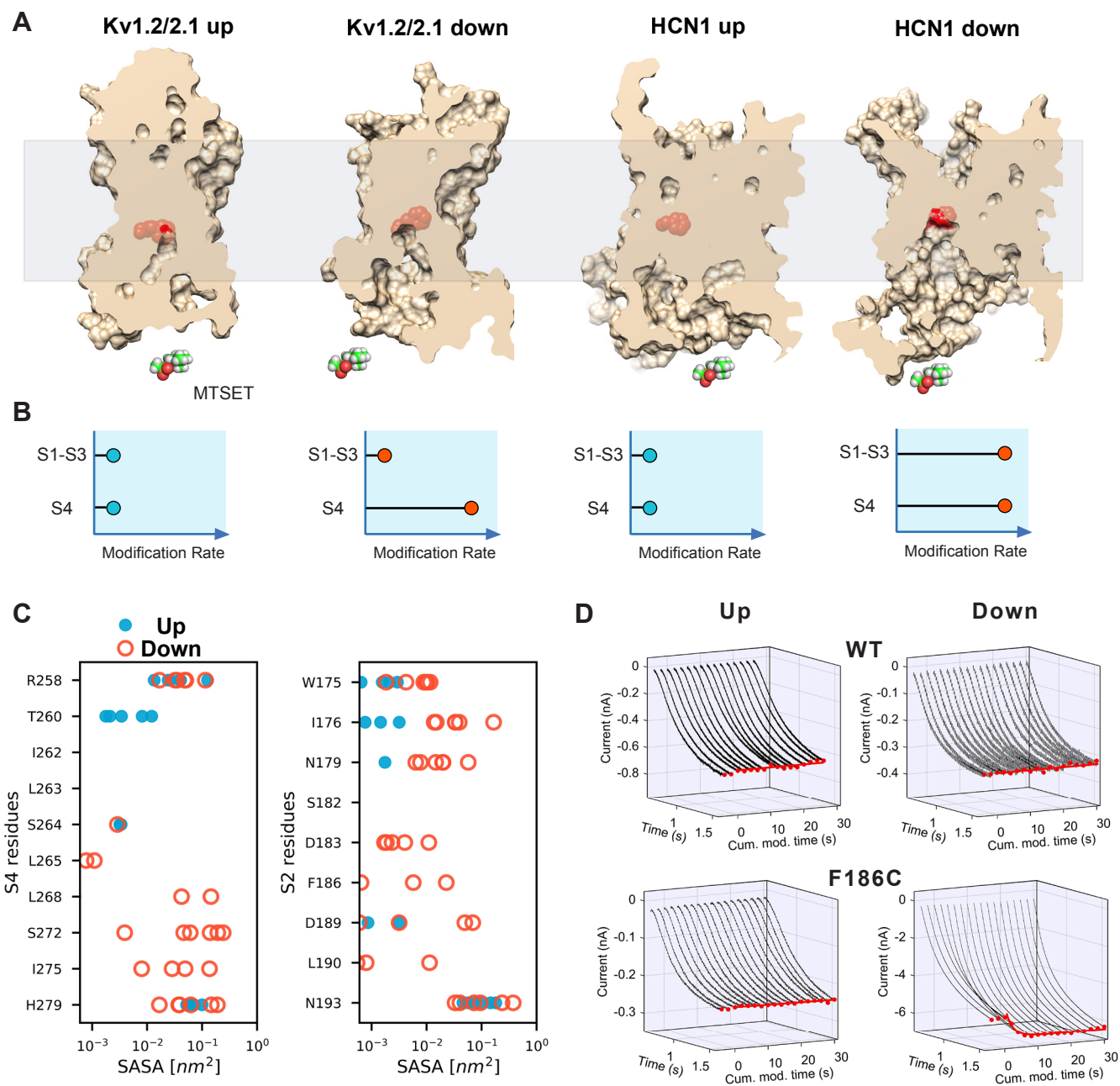


Figure 2

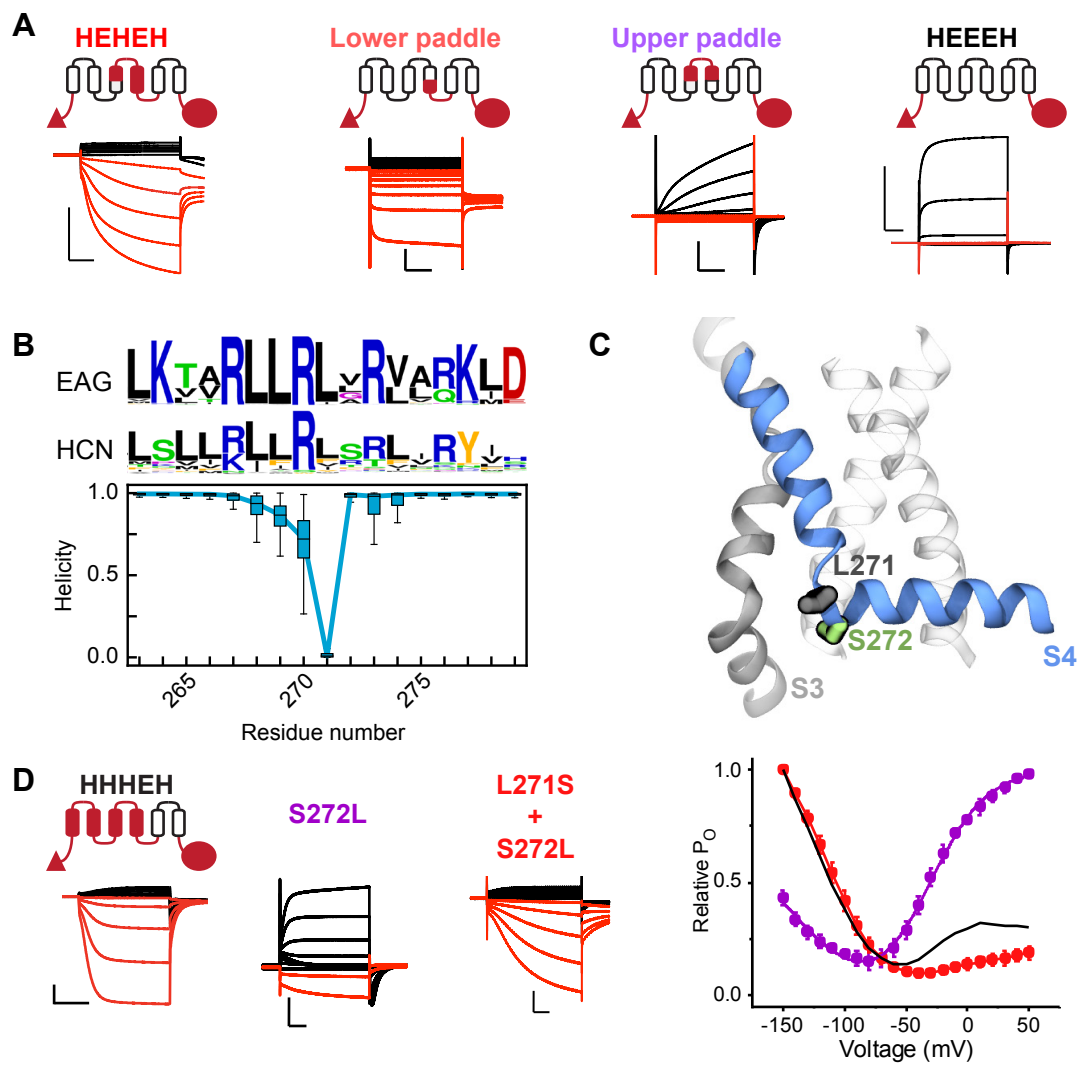


Figure 3

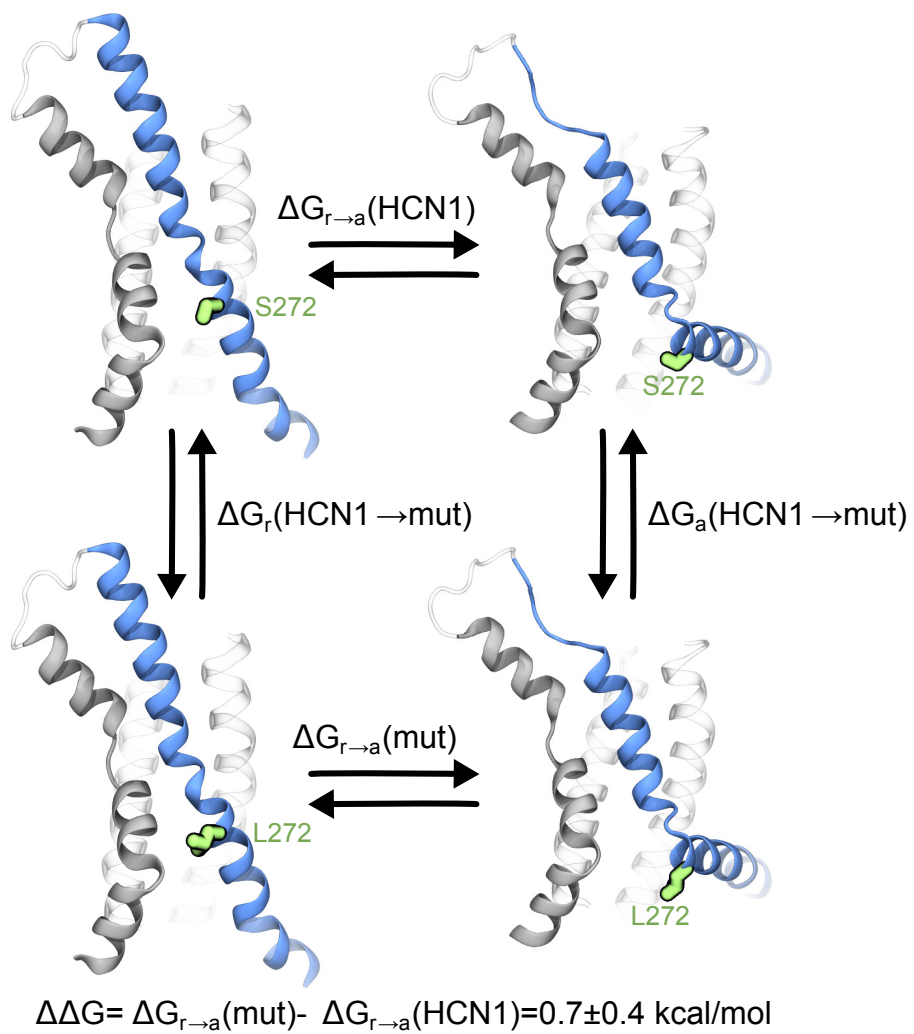


Figure 4

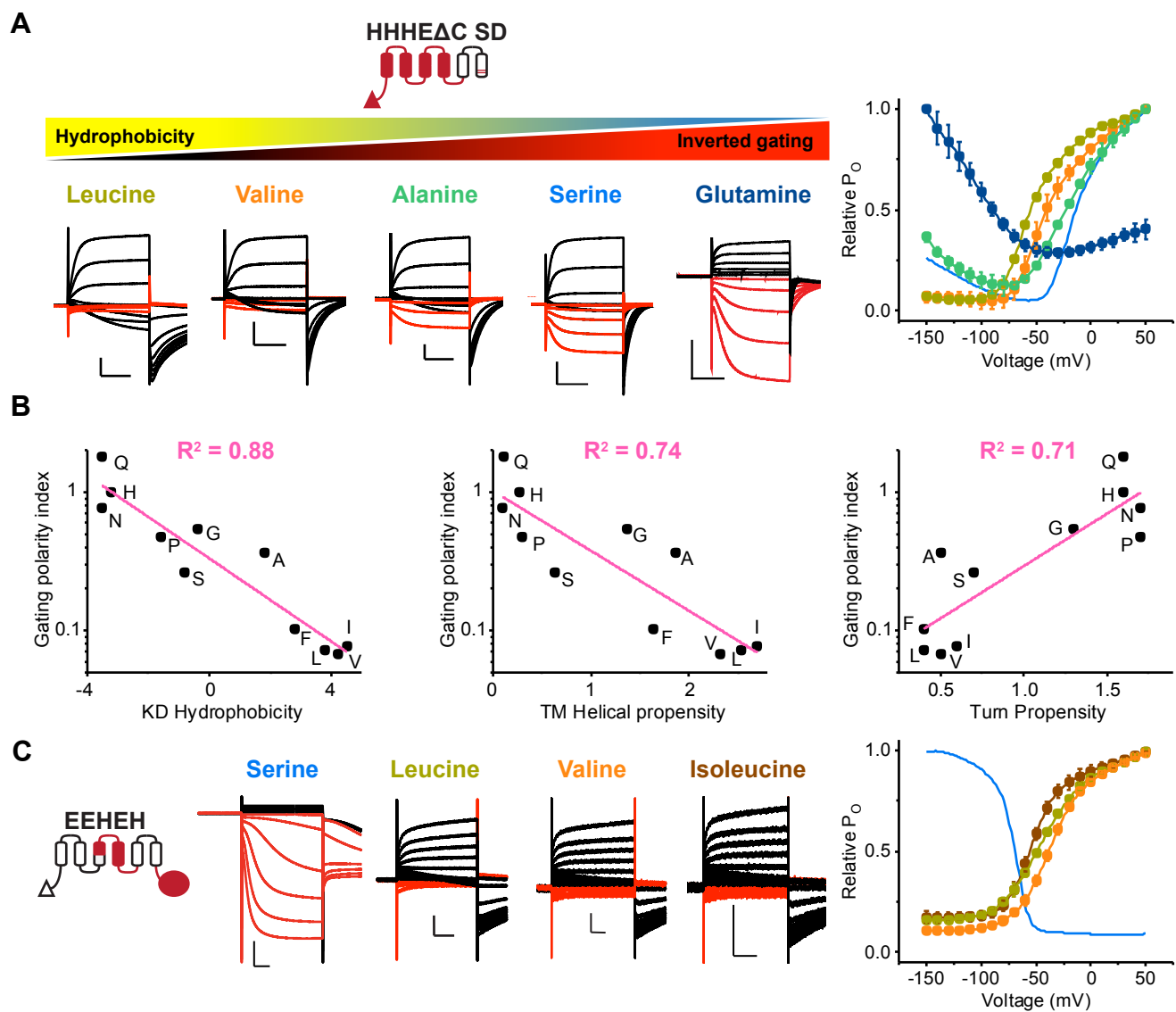


Figure 5

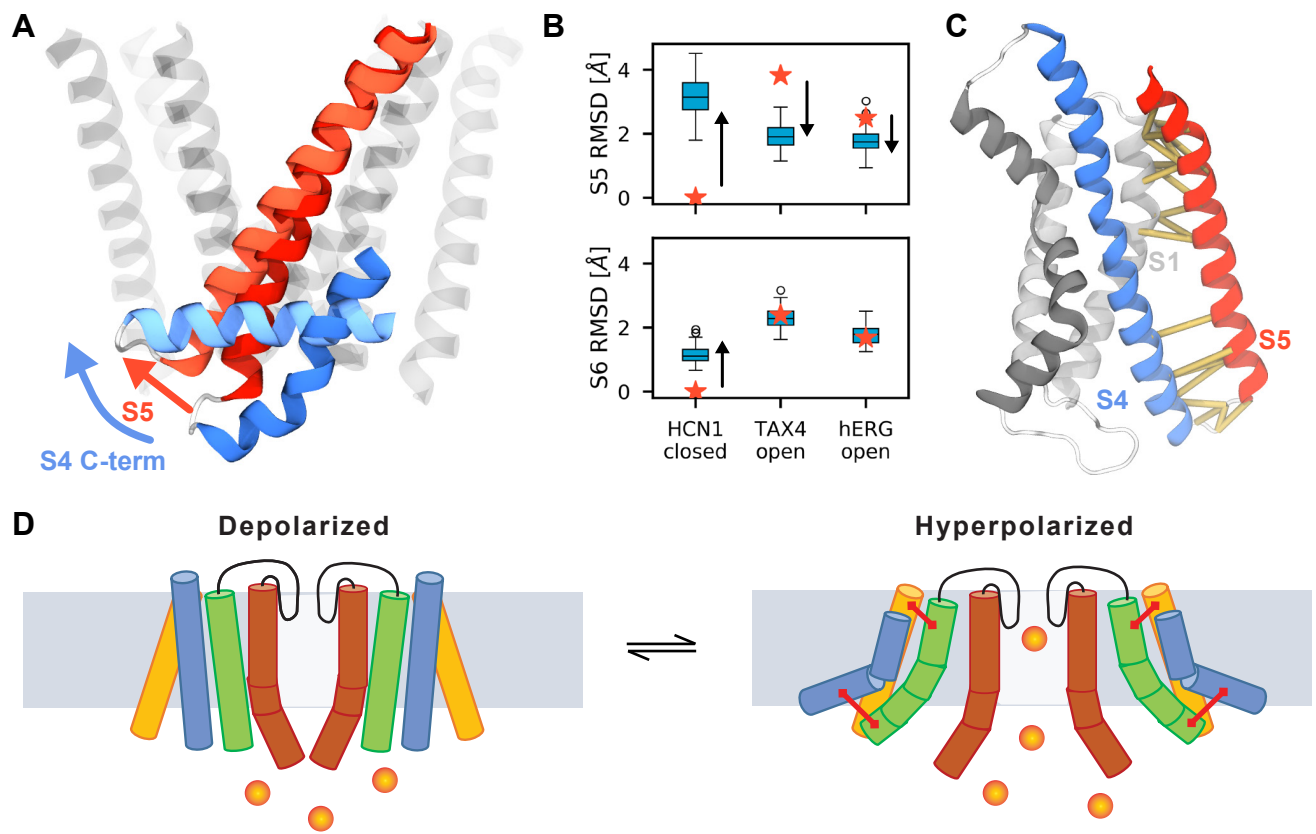


Figure 6

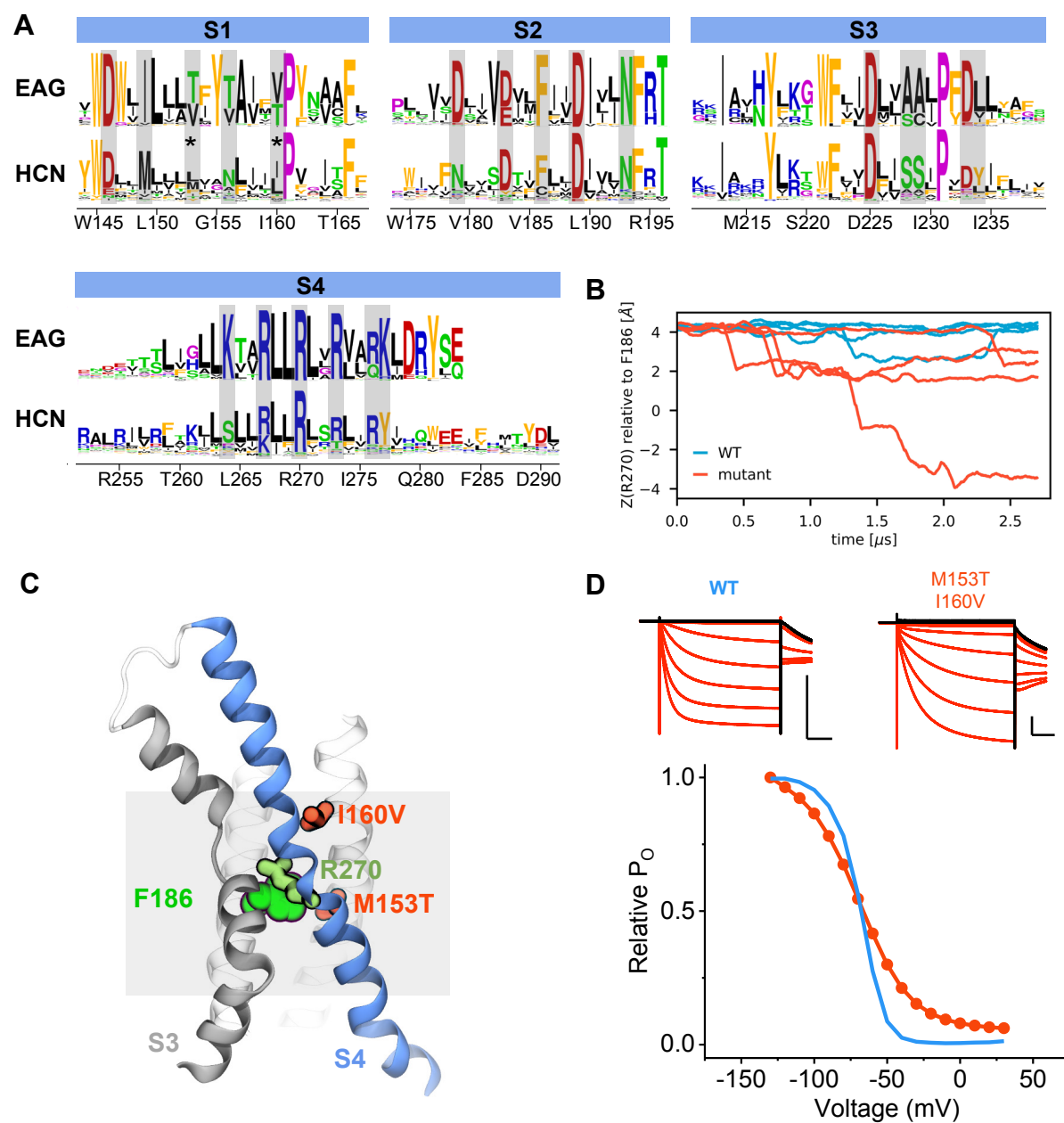


Figure 1 - Figure Supplement 1

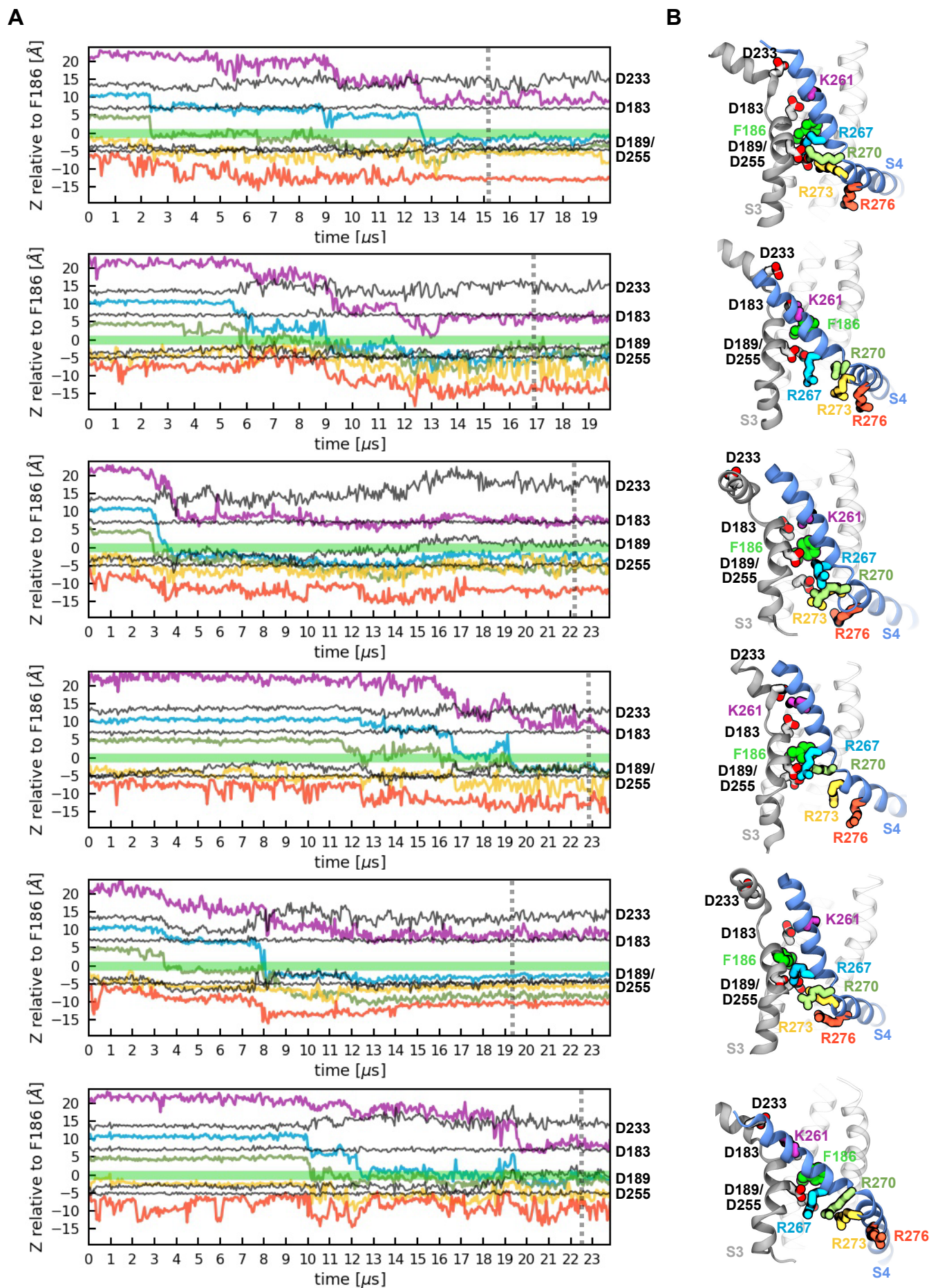


Figure 1 - Figure Supplement 2

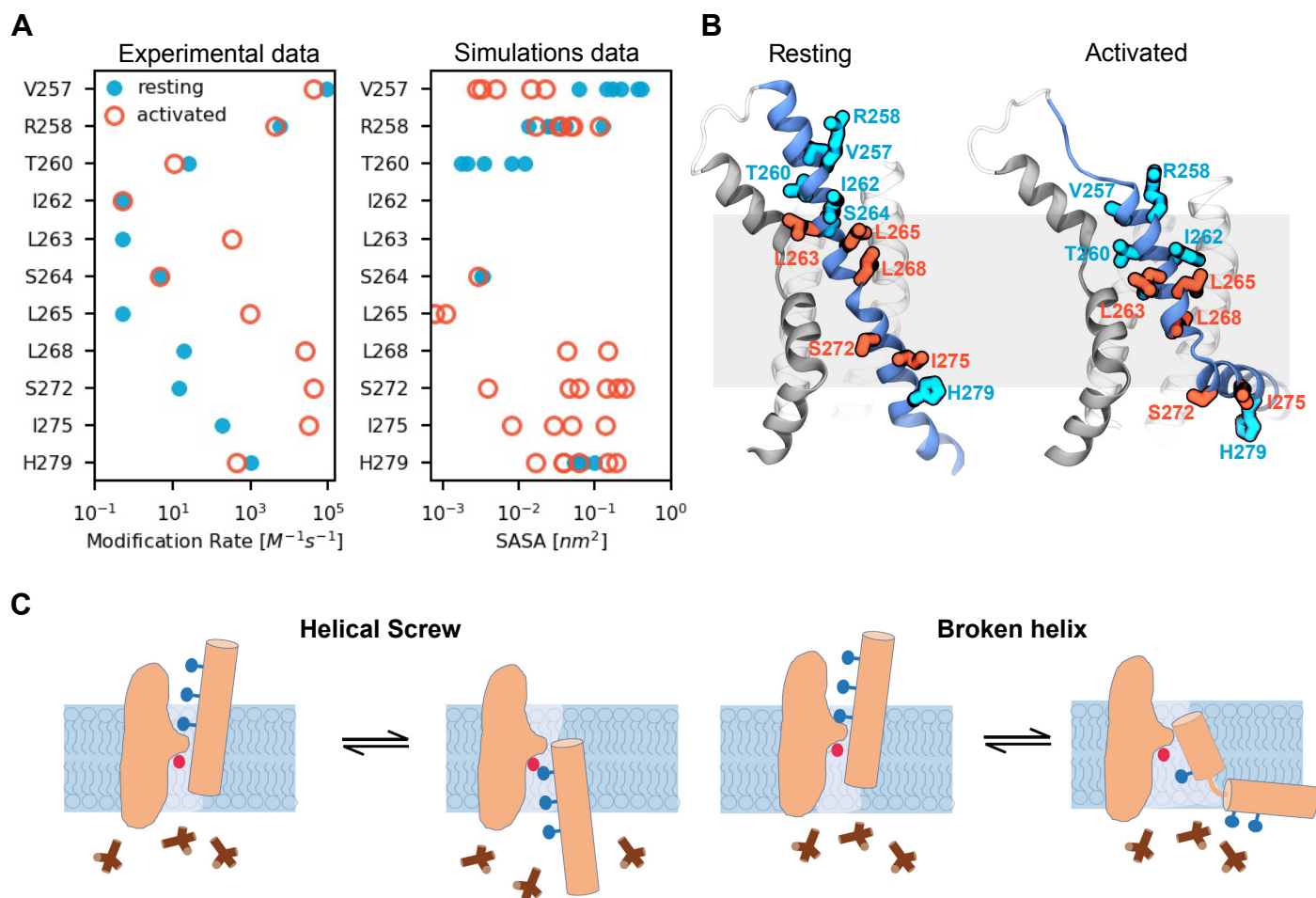


Figure 2- Figure Supplement 1

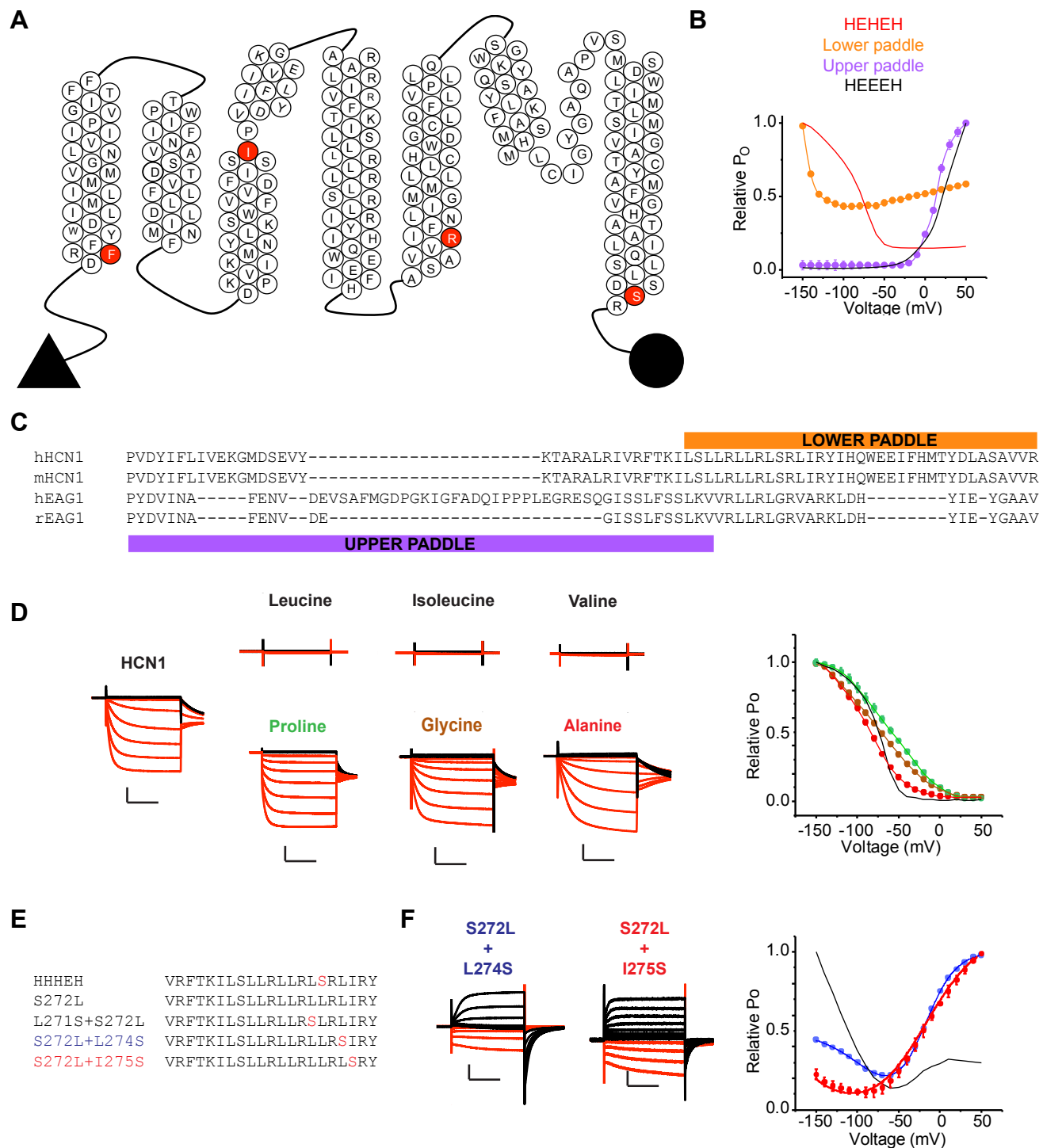


Figure 3 - Figure Supplement 1

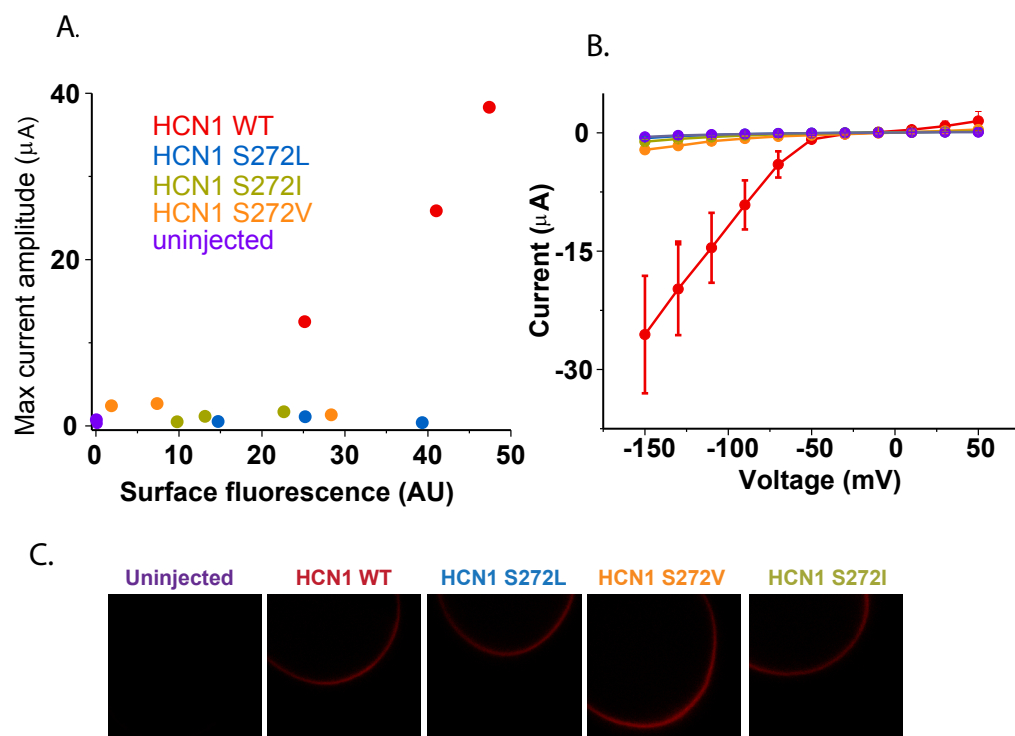
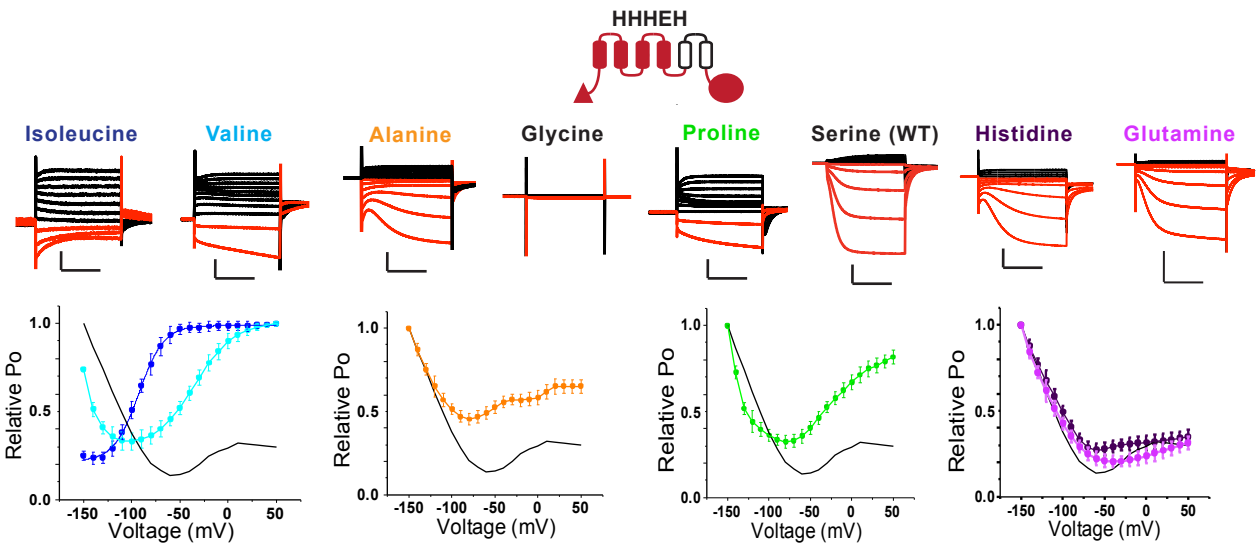
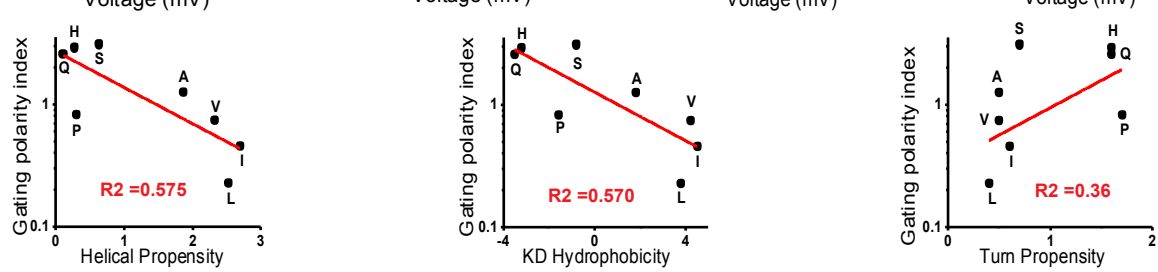


Figure 3 - Figure Supplement 2

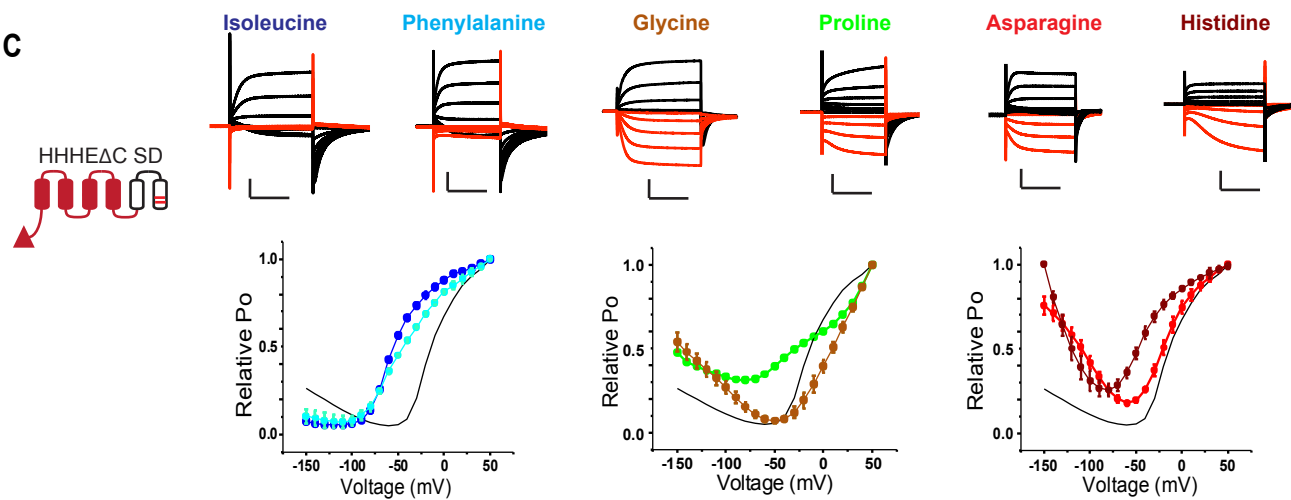
A



B



C



D

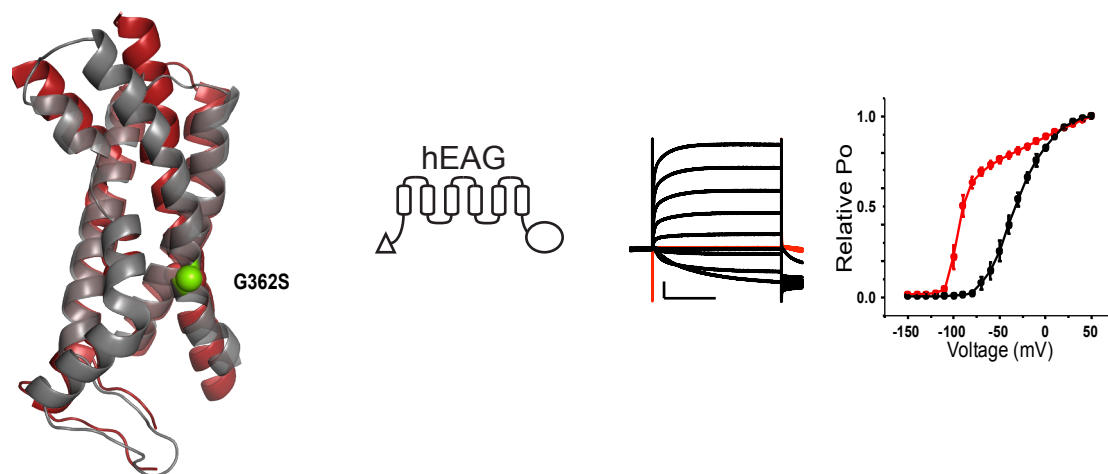


Figure 5 - Figure Supplement 1